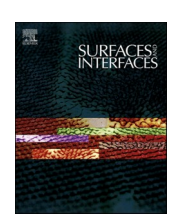
ELSEVIER

Contents lists available at ScienceDirect

Surfaces and Interfaces

journal homepage: www.sciencedirect.com/journal/surfaces-and-interfaces





Defect engineering in $ZnIn_2X_4$ (X=S, Se, Te) semiconductors for improved photocatalysis

Md. Habibur Rahman^a, Jiaqi Yang^a, Yujie Sun^b, Arun Mannodi-Kanakkithodi^{a,*}

- a School of Materials Engineering, Purdue University, 701 W Stadium Ave. West Lafayette, IN 47907, USA
- b Department of Chemistry, University of Cincinnati, Cincinnati, OH 45221 USA

ABSTRACT

 $ZnIn_2S_4$ has emerged as a material of interest for semiconductor-based chalcogenide photocatalysts due to its visible light absorption, chemical and thermal stability, and low cost. However, the photocatalytic activity of $ZnIn_2S_4$ is affected by the limited range of visible light absorption and ultrafast recombination of solar light-induced holes and electrons. While previous studies have considered the consequences of metal doping, metal deposition, and vacancy engineering on the photocatalytic activity of $ZnIn_2S_4$, a comprehensive understanding of native point defects and how they affect electronic and photocatalytic properties remains elusive. Here, we present a density functional theory (DFT) investigation of defect energetics in $ZnIn_2X_4$ (X=S, Se, Te) compounds in both bulk and ultrathin phases. Using both semi-local and hybrid DFT functionals, properties of interest such as the electronic band gap and band edges, optical absorption spectra, and carrier mobilities are first computed for defect-free structures. Although ultrathin $ZnIn_2S_4$ shows lower absorption compared to other chalcogenides, it exhibits sufficient overpotential for oxidation and reduction reactions for photocatalytic water splitting. Formation energies of all possible vacancies, self-interstitials, and anti-site substitutional defects are then computed for all structures, as a function of chemical growth conditions, charge state, and Fermi level (E_F), which leads to the identification of the lowest energy acceptor and donor type defects and their corresponding shallow or deep level nature. DFT results show that these metal sulfide photocatalysts are prone to Zn_{In} and In_{Zn} anti-site substitutions, which pin the equilibrium E_F close to the conduction band edge, indicative of n-type conductivity. While Zn_{In} does not create deep defect levels in $ZnIn_2X_4$, most of the stable native defects do create deep levels, which could adversely affect solar absorption. Finally, we report the influence of defects on

1. Introduction

With the rapid expansion of population and industrialization in the modern world, global energy supplies are being depleted, and a vast number of dangerous and poisonous chemicals are being emitted into the environment which has become a critical concern for human society's long-term survival [1-6]. There is an increasing focus on sustainable and eco-friendly solutions for dealing with global environmental pollution and energy shortages [1,6,7]. In this context, heterogeneous photocatalytic systems including semiconducting materials have emerged as a potential technology that can be used to not only smartly utilize solar irradiation to produce a variety of useful chemical fuels, such as hydrocarbons from CO2 conversion and H2 and O2 from photocatalytic H₂O splitting, but also to clean up the environment by degrading various harmful and toxic contaminants [1,8-13]. Due to their high photosensitivity, striking exciton binding energy, non-toxicity, low cost, and incredible photocatalytic activity, TiO2 and metal oxide semiconductors have received substantial

consideration in the field of green energy and environmental remediation [14–17]. However, certain constraints restrict their photocatalytic application, such as a wide bandgap ($TiO_2 \sim 3.2 \text{ eV}$ and $ZnO \sim 3.37 \text{ eV}$), fast recombination of photoinduced electron-hole pairs, and the fact that they only respond to ultraviolet (UV) light, meaning both TiO2 and ZnO can only use 3-5% of the total solar spectrum, severely limiting photocatalytic activity [1,3,6,7,17,18]. As a result, one of the key goals of current research has been to discover novel visible light-responsive photocatalysts to maximize the effective utilization of solar irradiation [19-21]. Metal sulfide compounds, as is well documented, are commonly employed as photocatalytic materials with a visible-light response, thanks to their narrow bandgap, and distinctive electronic and optical features [6,7,22-24]. ZnIn₂S₄, which belongs to the ternary series AB2X4, has recently emerged as a promising semiconductor photocatalyst for solar energy conversion and environmental purification [6.7.24.25].

There are two main crystalline phases reported for $ZnIn_2S_4$ in the literature, namely the hexagonal phase and the cubic phase. Hexagonal

E-mail address: amannodi@purdue.edu (A. Mannodi-Kanakkithodi).

 $^{^{\}ast}$ Corresponding author.

ZnIn₂S₄ has received greater attention in the domain of photocatalysis than the cubic ZnIn₂S₄ phase [6,7,25]. In 2003, Li and co-workers reported for the first time the hydrothermal fabrication of a novel ZnIn₂S₄ catalyst for photocatalytic H2O splitting, which piqued the interest of other photocatalysis experts [6,26]. Following that, there have been many studies on ZnIn₂S₄ from the perspective of photocatalytic H₂O splitting, hydrogen evolution reaction (HER), oxygen evolution reaction (OER), N₂ fixation, reduction of CO₂ to hydrocarbons, and pollutant removal [27-29]. Likewise, the efficient production of deuterated alcohols from carbonyls under the influence of visible light using ultrathin ZnIn₂S₄ as a photocatalyst has also been demonstrated [30]. Not only does ZnIn₂S₄ exhibit good light absorption characteristics and produce a large number of charge carriers when exposed to visible light, it also has optimal valence band (VB) and conduction band (CB) locations, as well as excellent reduction and oxidation capabilities, making it suitable for a variety of photocatalytic electrochemical reactions [7,31-34]. Additionally, for pollutant degradation and photocatalytic H2O splitting, a range of ZnIn₂S₄ nanomaterials with specific morphologies such as nanosheets, nanoribbons, nanowires (NW), and nanotubes (NT) have been reported [6,7,25]. Noticeably, the number of articles focusing on photocatalytic research on ZnIn₂S₄ and ZnIn₂S₄-based nanomaterials is steadily increasing every year, indicating that ZnIn₂S₄-based photocatalysts could be potential substitutes for ZnO and TiO2 [6,7]. However, the photocatalytic activity of ZnIn₂S₄ is still constrained owing to the limited range of visible light absorption and comparatively high recombination rate of solar light-induced holes and electrons [6,35-38]. Consequently, several modifications have been proposed, such as metal deposition, van der Waals (vdW) heterostructure configuration, metal doping, and vacancy engineering [6,30].

Defect engineering is a prominent way of altering the electronic and optical properties of semiconductors [39-45]. Defects are inevitable during the manufacturing process, especially when it comes to the synthesis of semiconductors. It is well understood that defects such as interstitials, substitutions, anti-sites, vacancies, grain boundaries, and surface states, may affect optoelectronic signatures and the performance of a photocatalyst [39,41,42,44,46-49]. It has been shown that introducing vacancies is an effective technique to enhance visible light absorption due to defect states forming near the Fermi level (E_F), which facilitates a more effective transfer of electrons from VB to CB [7,19,44]. However, vacancies also create more electron traps, reducing the transmission and longevity of photogenic carriers, and limiting the photocatalytic efficiency [6,7,22]. One of the most well-studied defects in metal oxide photocatalysts is the anion vacancy [6,7]. The potential of V_S (sulfur vacancy) to control the electronic structure and initiate unidirectional carrier flow has been extensively explored [7]. For example, Du et al. synthesized an ultrathin ZnIn₂S₄ and claimed that photogenerated electrons will be captured by the inserted V_S, thus weakening the overall electron-hole pair recombination [7,20]. Further, the overall oxidizing ability of holes is enhanced by the positive shift of the VB edge, facilitating more reducing electrons to engage in photocatalytic water splitting [7,20]. V_S can assist in creating an adaptive photocatalytic reaction system by not only efficiently separating photogenerated charge in space but also aiding in the preferred development of another functionalized group on the surface of ZnIn₂S₄ [6,7,20]. Cation vacancies can play a similar role in altering the electronic framework of the ZnIn₂S₄ photocatalyst. It was shown that increased V_{Zn} defects in ultrathin ZnIn₂S₄ resulted in enhanced charge density and efficient carrier transport [46]. Additionally, the photocatalytic CO₂ to CO reduction rate was recorded as $\sim 33.2 \text{ molg}^{-1}\text{h}^{-1}$, which was $\sim 3.6 \text{ times that of}$ $ZnIn_2S_4$ with a lower concentration of V_{Zn} [7,46]. Besides, V_{Zn} enhances the visible light response range of ZnIn₂S₄, speeds up carrier transport and separation, offers additional surface-active sites, and overall, boosts the photocatalytic performance of $ZnIn_2S_4$ [6,46].

Although there have been efforts to connect defects with the photocatalytic activity of $ZnIn_2S_4$, their ability to form and the effect of defect levels remain largely unexplained. Intrinsic point defects pin the

equilibrium E_F of a semiconductor in the absence of external impurities and thus determine the type of conductivity (n-type, p-type, or intrinsic) and charge carriers [50-52]. Predicting the electronic levels created by defects in photocatalysts is crucial for ensuring optimum optoelectronic performance. While shallow acceptor or donor levels near the band edges may not have any consequence on charge carrier recombination, deep defect levels can either be harmful or beneficial [53-62]. For example, deep defects can operate as non-radiative recombination centers for minority charge carriers, reducing their lifetime, obstructing carrier collection, and lowering optoelectronic efficiency [50-52]. In addition, defects can make the adsorption of species more or less feasible, and directly affect the catalytic performance [63]. Chalcogenide semiconductors exhibit a narrow band gap allowing them to absorb over 40% of the solar spectrum in the visible light range, and therefore, have been extensively employed as photocatalysts [63]. Since the discovery of graphene, research on two-dimensional (2D) ultrathin nanomaterials has grown exponentially as they offer unprecedented tunability of electronic, optical, and chemical properties compared to their bulk counterparts due to their ultrahigh surface-to-volume ratio [64]. Therefore, a comprehensive investigation of the stability of intrinsic point defects and their associated electronic levels in both bulk and ultrathin phases is quite important. The presence, types, and origin of defects in semiconductors can be determined experimentally using deep-level transient spectroscopy (DLTS), photoluminescence (PL), and cathodoluminescence (CL) spectroscopy [50-52]. However, due to difficulties in incorporating impurities or dopants in a given compound and assigning measured levels to specific defects, experimental methodologies are incomplete for a thorough characterization of defects and impurities in semiconductors [50–52]. On the other hand, density functional theory (DFT) computations are a valuable tool for simulating defects and have been widely used to estimate defect formation energies and corresponding charge transition levels in a variety of crystalline materials [50-52,65-67]. Also, we note that only ZnIn₂S₄ has been experimentally synthesized to date, while the other systems have not yet been fabricated yet. However, through our computational investigation, we aim to provide a deeper understanding of the properties of these promising metal chalcogenide photocatalysts and guide future experimental work on their synthesis and characterization.

In this work, we present a systematic first-principles investigation of the electronic, defect, and photocatalytic properties of bulk and ultrathin ZnIn₂X₄ (X=S, Se, Te) compounds. We begin with a discussion of the structure and optoelectronic properties of bulk ZnIn₂X₄ (bZnIn₂X₄) and ultrathin ZnIn₂X₄ (uZnIn₂X₄), following which we simulate all possible intrinsic point defects, i.e., vacancies, anti-sites, and interstitials (11 total defects) in supercells of bZnIn₂X₄ and uZnIn₂X₄. DFT computed total energies and reference energies yield all charge- and chemical potential-dependent defect formation energies, revealing deep/shallow defect levels and acceptor/donor type conductivity. Finally, we considered a stable donor-type defect in the ultrathin compounds and studied photocatalytic HER and OER by calculating the Gibbs free energy for each case and found that defective compounds yield lower energy barriers. Our computational framework and insights can serve as a guide for screening defects in any complex metal chalcogenide photocatalysts, such as CdIn₂X₄ and ZnGa₂X₄, to engineer photocatalytic properties.

2. Theoretical Methodology

All DFT computations were performed using the Vienna ab initio simulation package (VASP) [68]. The projector-augmented wave (PAW) pseudopotentials are employed to account for electron core interactions and exchange-correlation potential [69]. The exchange-correlation energy is approximated using the Perdew–Burke–Ernzerhof (PBE) functional within the Generalized Gradient Approximation (GGA) [70]. To account for the impact of on-site Coulomb interactions from Zn and In atoms, the Hubbard +U correction is implemented on top of GGA [21,

30]. Following prior work, U values of 4.5 eV and 5 eV are used for Zn and In, respectively [30]. All atomic configurations are completely relaxed until forces on all atoms were less than $0.05 \text{ eV/}\dot{A}$ while the plane wave energy cutoff is set at 500 eV [50-52,66]. Further, while modeling the uZnIn₂X₄ surface, to avoid interactions of uZnIn₂X₄ and its periodic image across the periodic boundary, we utilized a vacuum space of 2 nm perpendicular to the ultrathin compounds based on previous literature [5,71,72]. While modeling defects in the ultrathin sample, we considered only the (001) surface based on previous studies [73]. We acknowledge that unraveling the effect of surface termination on point defects requires a separate comprehensive study, and in this work, we focus only on how the native point defects energetics would vary from bulk to ultrathin state. To account for long-range van der Waals (vdW) interaction in the ultrathin compounds, the Grimme DFT-D3 method with zero damping function is employed [71,72,74]. Absorption spectra of bZnIn₂X₄ and uZnIn₂X₄ compounds are computed from the following equation [75]

$$\alpha(\omega) = \sqrt{2} \left(\sqrt{\varepsilon_1^2(\omega) + \varepsilon_2^2(\omega)} - \varepsilon_1(\omega) \right)^{\frac{1}{2}}$$
 (1)

where $\alpha(\omega)$ is the absorption coefficient as a function of incident photon frequency ω , and $\epsilon_1(\omega)$ and $\epsilon_2(\omega)$ is the real, and imaginary part of the dielectric function, respectively.

In the case of the bZnIn₂X₄, phase, a gamma-centered $3 \times 3 \times 3$ k-point mesh is used to perform geometry optimization, followed by the electronic density of states (DOS), point defect, and dielectric function calculations on a 56 ± 1 (i.e., 56 for pure cell and anti-sites, 55 for vacancy, and 57 for interstitial) atom-based $2 \times 2 \times 1$ supercell [5]. The k-point convergence test is carried out to ensure the number of k-points is sufficient (Table S1). For modeling the uZnIn₂X₄, phase, all of the necessary calculations are carried out on a 56 ± 1 atom-based $2 \times 2 \times 1$ unit cell with a gamma-centered $3 \times 3 \times 1$ k point mesh. The following equations are used to compute the formation of enthalpy E^f of a defect as a function of the Fermi level (E_F), and any defect transition level [52,76], $\varepsilon(q_1/q_2)$.

$$E^{f}(D^{q}, E_{F}) = E(DZnIn_{2}X_{4}^{q}) - E(ZnIn_{2}X_{4}) + \mu + q(E_{F} + E_{VBM}) + E_{corr}(2)$$
(2)

$$\varepsilon(q_1/q_2) = \frac{E^f(q_1, E_F = 0) - E^f(q_2, E_F = 0)}{q_2 - q_1}$$
(3)

In Eq. (2), $E(ZnIn_2X_4)$ is the total DFT energy of either $bZnIn_2X_4$ or $uZnIn_2X_4$, and $E(DZnIn_2X_4^q)$ refers to the total DFT energy of supercells containing defect D (i.e., vacancy, interstitial, or anti-site) in a charge state q, E_{VBM} corresponds to the valance band maximum (VBM) calculated from electronic DOS (before shifting the E_F to zero) of the defectfree sample, and E_{corr} refers to the charge correction energy calculated by implementing the scheme of Freysoldt et al. [76] in order to account for the periodic interplay between the defect and its image. E^f is a function of E_F and q, such that the slope of the E^f vs E_F plot is equal to q[51,76]. We note that due to the confinement to a smaller volume, thin films can extend the effects of finite size. The existence of surfaces or interfaces in thin films could potentially alter the defect characteristics and have an impact on the electrostatic interactions between the defect and its image in the periodic supercell. To effectively account for finite-size effects, using a very large supercell is highly recommended. By simulating the defect at several potential sites throughout the thin film, it is possible to account for the effect of surfaces or interfaces on charged defects. However, in this study, we only focus on identifying low-energy stable defects qualitatively, although we acknowledge that results may vary quantitively in different modeling approaches, for example, using even larger supercells, or considering other potential defect sites.

For any $DZnIn_2X_4$ cell, all chemical potentials are defined in terms of the elemental standard states of Zn, In, and X, as well as the formation

energy of their binary or ternary compounds. All chemical potentials are constrained to maintain thermodynamic equilibrium for ZnIn₂X₄ and prevent decomposition to ZnX, InX, and In₂X₃ binary compounds [30]. These requirements can be written as: $\Delta\mu_{Zn} + 2\Delta\mu_{In} + 4\Delta\mu_{X} = \Delta H$ (ZnIn₂X₄), $\Delta\mu_{Zn} + \Delta\mu_{X} < \Delta H(ZnX)$, $\Delta\mu_{In} + \Delta\mu_{X} < \Delta H(InX)$, and $2\Delta\mu_{In} +$ $3\Delta\mu_X < \Delta H(In_2X_3)$. Here, $\Delta H(ZnIn_2X_4) = E(ZnIn_2X_4) - E(Zn) - 2E(In) - 2E(In)$ 4E(X), $\Delta H(ZnX)=E(ZnX)-E(Zn)-E(X)$, $\Delta H(InX)=E(InX)-E(In)-E(X)$, and $\Delta H(In_2X_3) = E(In_2X_3) - 2E(In) - 3E(X)$. Note that E(system) indicates the total energy per formula unit (p.f.u.) of the associated system after DFT optimization. The chemical potentials of Zn, In and X are referenced to their respective elemental standard states such that μ_{Zn} = $\Delta\mu_{Zn}+$ E(Zn), μ_{In} = $\Delta\mu_{In}$ + E(In), and μ_{X} $_{=}$ $\Delta\mu_{X}+$ E(X). We considered 3 chemical potential conditions, namely, In-rich, X-rich, and moderate, i. e., somewhere in the middle of the cation and anion-rich growth conditions, and reported defect formation energies for each based on the given restrictions. In the neutral and charged states (q = +3, +2, +1, 0, -1, -2, -3), the supercell shape and size are kept fixed (viz., the lattice parameters are not allowed to change considering the point defect is dilute enough to not alter the X-ray diffraction pattern) while DFT optimization is performed [66]. Generally, multiple states of charge can exist while defects emerge spontaneously in semiconductors, which means electrons from the charged defects could occupy the energy levels within the bandgap [77]. Consequently, thermodynamic transition levels (TTL) occur at the value of E_F where the E^f of two different charge states for the same defect coincide, relating to transitions from one charge state to another, and corresponding transition levels are determined using [77] $\varepsilon(q_1/q_2)$.

To simulate the photocatalytic HER/OER reaction on the surface of uZnIn₂X₄, Gibbs free energy is calculated using Eq. 4 [72], $\Delta G = \Delta E_{ads} + \Delta ZPE - T\Delta S + \Delta G_U$ (4), where ΔE_{ads} =E(product) - E(reactant), ΔZPE and $T\Delta S$ refer to change in zero point energy and entropy energy, respectively, between the product and reactant while the temperature is set as 298.15 K[72]. ZPE is calculated using ZPE= $\frac{1}{2}\sum hv_i$, where v_i refers to the vibrational frequency of either free H₂/O₂/H₂O placed in a large simulation box, or H/O/OH/OOH species adsorbed on the catalyst. Note that while computing the vibrational frequency of the adsorbed H/O/OH/OOH species, the whole catalyst is kept fixed, and the H/O/OH/OOH atoms are free to vibrate along all directions [72]. En-

tropy S is calculated from the following equation [72]: $S(T) = \sum_{i=1}^{3N} \left[-\frac{1}{2} \right]$

 $Rln\left(1-e^{-\frac{hv_i}{K_BT}}\right)+\frac{N_Ahv_i}{T}\frac{e^{-\frac{hv_i}{K_BT}}}{1-e^{-\frac{hv_i}{K_BT}}}\right]$, and U is the external electrode potential.

3. Results and Discussion

3.1. Characterization of optoelectronic properties

We first performed ab-initio molecular dynamics (AIMD) simulations at 300 K to confirm the stability of all compounds at room temperature [78]. During AIMD simulations, the NVT (constant atom, volume, and temperature) ensemble is employed with a Nose-Hoover thermostat to maintain the temperature of the system [78]. For all the atoms, quantum mechanics-driven equations of motions are integrated with a 1 fs time step up to 5 ps [78]. The crystal structures of bZnIn $_2$ S4 and uZnIn $_2$ S4 after 5 ps of AIMD simulations are shown in Fig. 1(a-b), indicating that both compounds are stable at 300 K. The total energy evolution during the AIMD simulation has also been displayed in Fig. 1(c), which confirms the energetic stability of both bulk and ultrathin phases.

Table 1 provides the DFT-optimized lattice parameters of all the structures including the thickness of $uZnIn_2X_4$, showing that lattice constants and thickness increase as the atomic weight of X increases. Accurately estimating the electronic bandgap, the bandgap type (direct or indirect), and the contribution of various species to the electronic

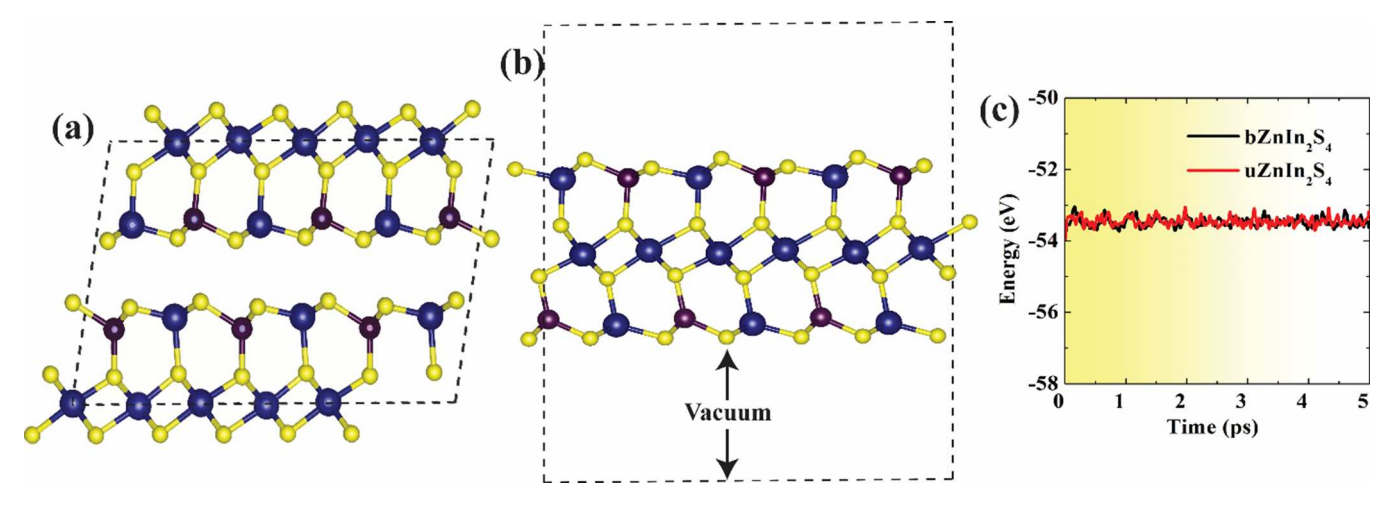


Fig. 1. (a) Optimized atomistic structures of of (a) $bZnIn_2S_4$, and (b) $uZnIn_2S_4$ (001) from AIMD simulation at 300 K after 5 ps, and (c) energy spectrum during AIMD simulation at 300 K. Dark brown, navy blue and yellow colors depict the Zn, In and S atoms respectively. (For interpretation of the references to colour in this figure legend, the reader is referred to the web version of this article.)

Table 1
The optimized lattice parameters, slab thickness, bandgap, band edges, and electron effective mass m_e^*/m_0 of all bulk and ultrathin compounds. Labels D and I refer to direct and indirect bandgaps, respectively.

Compounds	a_0 (Å)	b_0 (Å)	c_0 (Å)	thickness (Å)	Bandgap, GGA+U (eV)	Bandgap, HSE06 (eV)	m_e^*/m_0	VBE, HSE06 (eV)	CBE, HSE06 (eV)
bZnIn ₂ S ₄	6.70	3.87	13.00	-	1.84 (I)		0.22	-	-
bZnIn ₂ Se ₄	7.09	4.06	1 3.80	-	1.12 (I)		0.15	-	-
bZnIn ₂ Te ₄	7.57	4.37	14.65	-	0.68 (I)		0.34	-	-
$uZnIn_2S_4$	6.68	3.87	-	9.48	2.16 (D)	3.0 (D)	0.23	-5.94	-2.94
uZnIn ₂ Se ₄	7.01	4.06	-	10.12	1.45 (I)	2.20 (I)	0.18	-7.97	-5.81
$uZnIn_2Te_4$	7.56	4.37	-	10.98	0.81 (I)	1.42 (I)	0.75	-6.86	-5.45

density of states (DOS) is crucial to evaluating a material's suitability for optoelectronic and photocatalytic applications [78-80]. It is well known that the semi-local GGA-PBE functional will underestimate the bandgap of solids, and the non-local Heyd-Scuseria-Ernzerhof-06 (HSE06) functional could provide a more accurate estimate. However, HSE06 calculations are significantly more expensive than GGA. On the other hand, the GGA+U approach, typically used to correct for self-interaction energy in elements with d and f orbitals by adding an additional Coulomb interaction term, could be used to align the theoretical and experimental bandgaps of the Zn-based chalcogenides being studied here [79]. The electronic band structure of all the compounds from GGA+U calculations is presented in Fig. 2, and the corresponding bandgap and type of bandgap have been summarized in Table 1 for all the crystals. Additionally, for benchmarking, GGA+U relaxed structure is fed into the HSE06 functional to only simulate the electronic bandgap of the ultrathin compounds to accurately report the band edge position with respect to the vacuum (HSE06 band structures are added to Fig.S7).

GGA+U band structures show that all the compounds are semi-conductors, with the bandgap reducing as X goes from S to Se to Te. It is noteworthy that uZnIn₂X₄ compounds have a higher bandgap than their bulk counterparts, similar to hexagonal TMDC materials, e.g., MoS₂, MoSe₂, WS₂, and WSe₂ (the GVJ-2e bandgap of bulk hexagonal MoS₂, MoSe₂, WS₂, and WSe₂ are \sim 1.23 eV, \sim 1.09 eV, \sim 1.32 eV, and \sim 1.21 eV, while the corresponding bandgap for ultrathin phases are \sim 1.88 eV, \sim 1.57 eV, \sim 2.03 eV, \sim 1.67 eV, respectively [80]), meaning that they could be used in a range of photocatalytic applications [81–83]. Except for uZnIn₂S₄, we observe indirect band gaps for all bulk and ultrathin systems [82]. In bZnIn₂X₄ systems, the conduction band edge (CBE) and valence band edge (VBE) is found to be parabolic and flat respectively, which suggests free electrons, and strongly localized holes in the conductions bands (above the E_F) and valence bands (below the E_F),[84].

Further, using the expression $m_e^*/m_o=\hbar^2\left[\frac{\partial^2 E(\kappa)}{\partial \kappa^2}\right]^{-1}$, the effective masses

of electrons, m_e^*/m_o have been determined from the curvature of the CBM at the $\Gamma-Z$ and $\Gamma-X$ directions of the bZnIn₂X₄ and uZnIn₂X₄ compounds [85], respectively, and corresponding data are summarized in Table 1. Low m_e^*/m_o of bZnIn₂S₄, bZnIn₂Se₄, uZnIn₂Se₄, and uZnIn₂Se₄ suggest high carrier mobility in these semiconductors indicating suitability for optoelectronic applications[86,87]. It is worth noting that X states dominate the VBM region, where the DOS is generally larger than the CBM region which contains both In and X states, as shown in the projected density of states (PDOS) in Fig. 3.

In the context of photocatalytic reactions, an electron (e-) in the VB is excited to the CB by a photon while a hole (h+) is left in the VB. This eventually leads to formation of a photo-excitation state and the creation of electron-hole pairs [75,88,89]. Subsequently, this excited electron may be utilized not only to reduce an acceptor like H^+ but also to oxidize donor molecules such as H₂O with a hole [75,89-91]. Generally, several requirements must be met for photocatalytic H2 generation on the surface of a semiconductor via the H₂O-splitting process [86,87,92]: (1) the energy of the CBE must be equal to or greater than -4.44 eV from the vacuum (reducing potential) for generation of H₂ by a reduction process (H⁺/H₂), (2) the energy of VBE must be lower than or equal to -5.67 eV from the vacuum (oxidizing potential) for producing O2 by an oxidation reaction of H₂O (O₂/H₂), (3) semiconductor must have a bandgap of 1.23 eV or higher, (4) semiconductor must have notable absorption peaks in the near UV and visible regions to utilize much of the solar energy spectrum, and (5) it should have a large surface to volume ratio to accommodate the photocatalytic reaction process. In that context, the relative band edge position of uZnIn₂X₄ with respect to vacuum has been evaluated using HSE06 computations, and corresponding data are provided in Table 1. The band edge position was computed using the work function Φ , which is the difference between the E_F and the vacuum level, based on the equations [93], CBE= $-\Phi + \frac{1}{2}E_g$ and VBE= $-\Phi - \frac{1}{2}E_g$, where E_g is the electronic bandgap of the respective sample. It is clear

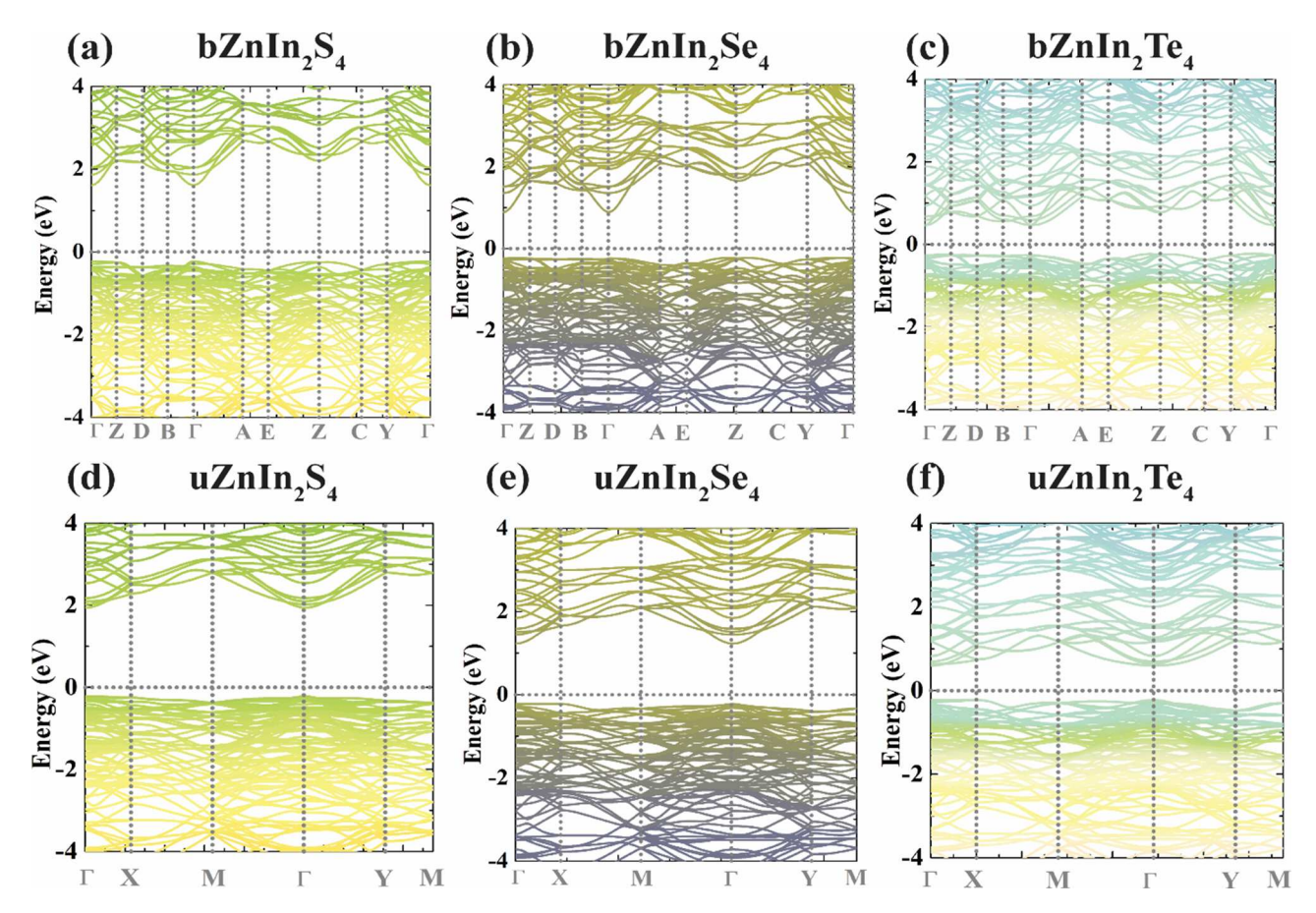


Fig. 2. Electronic band structures of (a) bZnIn₂S₄, (b) bZnIn₂Se₄, (c) bZnIn₂Te₄, (d) uZnIn₂Se₄, (e) uZnIn₂Se₄, and (f) uZnIn₂Te₄ from GGA+U.

that $uZnIn_2S_4$ holds great promise for photocatalytic H_2O splitting as this ultrathin sample exhibits sufficient overpotential for oxidation and reduction reactions for photocatalytic H_2O splitting. Furthermore, the computed optical absorption coefficients as a function of incident photon energy are plotted for all compounds in Fig. 4(a). It is evident that although all the compounds demonstrate an absorption peak in the UV range (> 2.75 eV), they also exhibit good absorption in the visible region (380 nm–700 nm). To gain further insight into absorption in the visible range, the absorption coefficient as a function of wavelength is presented in Fig. 4(b). It is clear that $bZnIn_2X_4$ shows higher absorption compared to the $uZnIn_2X_4$ counterparts, in good agreement with prior studies of ultrathin MoS_2 where absorption increases as the thickness of the compounds increases [94]. It should be noted that all the compounds show good absorption in the low-energy region as X changes from S to Se to Te.

3.2. Characterization of native point defects

It has been reported that point defects could boost the conductivity in metal sulfide photocatalysts [44]. E.g., cation defects may offer an enhanced p-type conductivity due to the movement of holes through a mutual shifting of VBE and CBE, as well as trap states which could potentially increase the carrier lifetime [44]. However, cation defects may occasionally result in the formation of new intermediate bands within the bandgap. Overall, incorporating cation defects in a photocatalyst could be beneficial [44], such as by (1) improving the overall electronic conductivity, (2) increasing electron mobility and interfacial charge transfer, leading to low recombination rates and high photocatalytic activity, and (3) forming a large number of active sites on the photocatalyst surface. At the same time, it is widely known that vacancies are the most common defects in a variety of photocatalytic

materials. These defects may have a major impact on the material's electronic properties as well as surface adsorption/desorption characteristics, improving or hindering its photocatalytic performance.

We rigorously simulated all possible native point defects, namely vacancy (V_{Zn.} V_{In}, V_X), self-interstitials (Zn_i, In_i, and X_i), and anti-site substitution (Zn_{In} , Zn_{X} , In_{Zn} , In_{X} , X_{In}) in both the bulk and ultrathin ZnIn₂X₄ phases. The DFT-computed E^f as a function of the E_F is presented in Fig. S2-S7 in 3 different growth conditions as mentioned in the methodology section. Note that E_F varies from VBM to GGA+U projected CBM. For easier visualization, and acknowledging the fact that higher energy defects are less likely to form, we present energetics for the lowest energy acceptor and donor type defects in Fig 5. Before going further, we acknowledge that standard semi-local functions like GGA or GGA+U, may not yield accurate band gaps [67]. For example, previous reports show that the bandgap of AlN and GaN is underestimated by 34%, and 55%, and InN is predicted to be metallic instead of a semiconductor [67]. Defect formation energies and transition levels may also be impacted by band-gap errors of this scale [67]. However, it has been reported that defect charge transition levels from semi-local functionals often compare favorably with experiments for a variety of semiconductor classes, including hybrid perovskites and even group IV, III-V, and II-VI semiconductors [66]. This distinction can be explained by the fact that total energy differences in DFT are more precise than Kohn-Sham energy levels used for estimating band edges or band gaps [66]. Alternatively, in the case of hybrid perovskites, an unexpected canceling of errors results in GGA being as precise as HSE06+SOC (spin-orbit coupling). Previous research has shown that defect levels computed from semi-local GGA for well-known ZB semiconductors like Si and GaAs can span the material's physical band gap; in other words, the defect transition levels calculated from GGA correlate well with experimental data up to the experimental band gap [95,96]. For

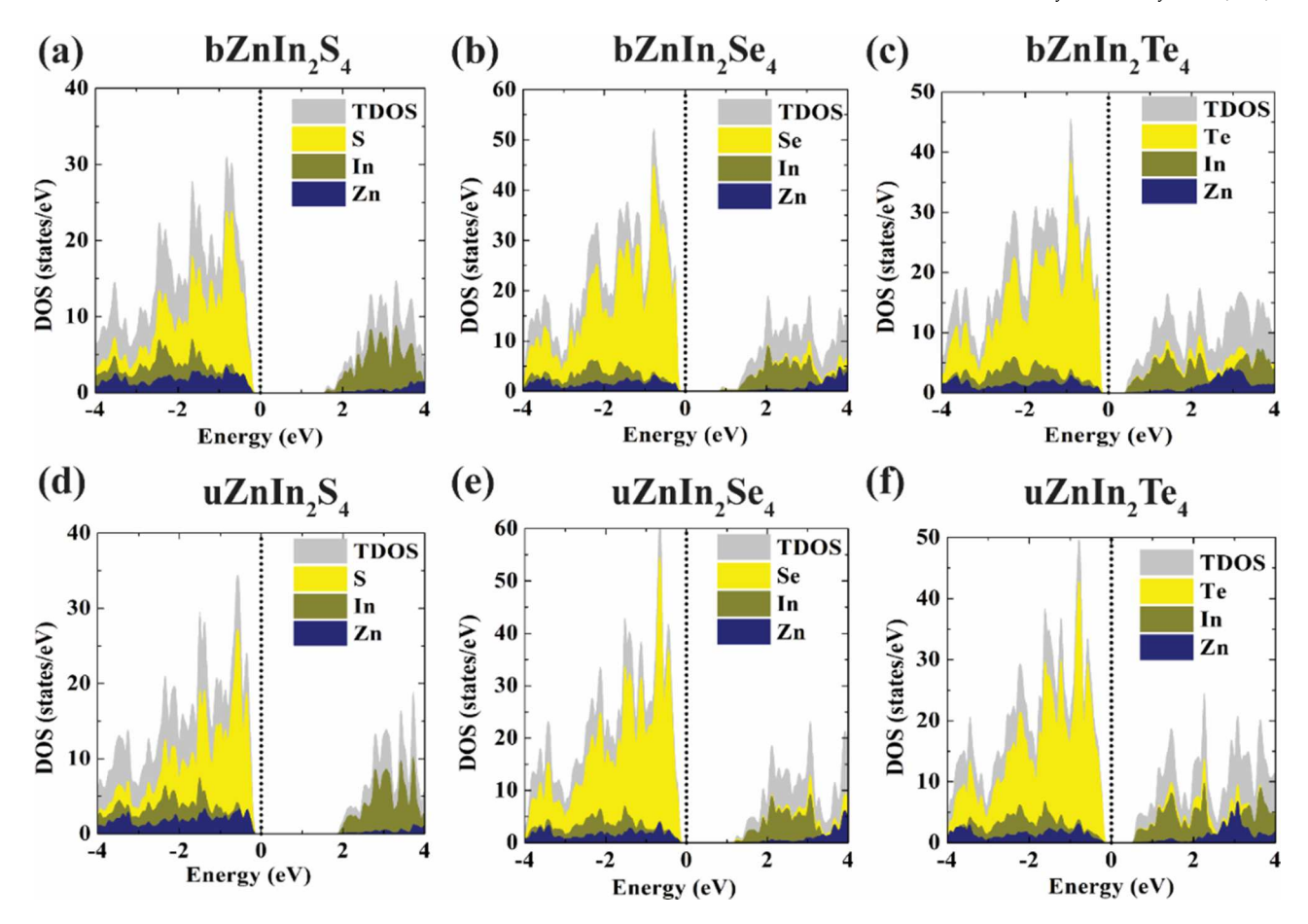


Fig. 3. Projected electronic DOS of (a) $bZnIn_2S_4$, (b) $bZnIn_2Se_4$, (c) $bZnIn_2Te_4$, (d) $uZnIn_2Se_4$ (e) $uZnIn_2Se_4$ and (f) $uZnIn_2Te_4$ from GGA+U. E_F is denoted by the dotted line.

example, the experimentally measured defect levels of V_{Cd} (-1/-2), Cu_i (+1/0), and Te_{Cd} (+2/+1) in zincblende CdTe are ~ 0.43 eV, ~ 1.08 eV, ~0.35 eV, respectively, whereas the computed defect level from GGA are ~ 0.35 eV, ~ 1.06 eV, ~ 0.38 eV, providing some confidence in the GGA predictions [52]. Going forward, any transition level that occurs at an $E_F > 0.2$ eV away from the band edges is referred to as "deep," whereas transition levels close to the band edges (either VBM or CBM) have been denoted as "shallow." It should be noted that "deep" electronic levels caused by energetically favorable defects within the bandgap of a semiconductor may have a negative impact on photovoltaic (PV) efficiency by causing non-radiative charge carrier recombination and lowering overall efficiencies [50]. Shockley-Read-Hall theory predicts that defect trap states in the center of the band gap have a far higher charge carrier trapping rate than shallow defect states [50]. However, earlier studies have indicated that energy levels in the band gap can be employed as intermediate bands to aid the absorption of sub-gap photons, which could theoretically increase the absorption efficiency [52].

From Fig. 5(a), it can be seen that V_{Zn} might act as both a deep donor and acceptor in bZnIn₂S₄, exhibiting two transition levels within the bandgap, ϵ (+2/0) = 0.71 eV and ϵ (0/-2) = 1.41 eV. V_{Zn} acts as an amphoteric defect, which can be credited to the multiple oxidation states of Zn as well as neighboring X and In atoms. Under both n-type (E_F close to CBM) and p-type (E_F close to VBM) conditions, V_{Zn} is quite stable, while under intrinsic (E_F close to the middle in the bandgap) conditions, the formation of V_{Zn} is unlikely because of its higher formation energy. Similarly, owing to various possible oxidation states of In (e.g., +3 and +1), we found that V_{In} might also act as an amphoteric defect in bZnIn₂S₄ with various charge transition levels such as ϵ (+3/+1) = 0.16 eV, ϵ (+1/-1) = 0.31 eV, and ϵ (-1/-3) = 1.15 eV. Although the formation energy of V_{In} is relatively high under p-type conditions,

the existence of V_{In} is more likely under n-type conditions due to its low formation energy near the CBM. These results are in agreement with previous point defect studies in GaN [67], where metal vacancy also acts as an amphoteric defect similar to V_{Zn} and V_{In} in bZnIn₂S₄. Interestingly, from our DFT calculations, V_{S} has not been identified as a stable defect in bZnIn₂S₄ under any conditions (readers are directed to the SI), and therefore, the formation of V_{S} in bZnIn₂S₄ is either unlikely or it would exist in a very low concentration unless we intentionally increase the

concentration ($C(D^q)=e^{-\left(rac{B^f(D^q)}{k_BT}
ight)}$, the Boltzmann distribution law implies that higher the formation energy, lower the concentration of the defect [40]). This shows good agreement with recent experimental reports indicating that the ESR (electron spin resonance) signal associated with the intrinsic V_S in $bZnIn_2S_4$ could not be detected [28]. V_{Zn} is more likely to form in bZnIn₂S₄ under p-type or n-type conditions and would act as an electron acceptor which is also in agreement with prior experimental studies indicating that V_{Zn} could respond as an electron acceptor, and eventually enhance the separation of electrons from holes [46]. Our DFT data also suggest that Zn_{i} could act as a shallow donor with a transition level ε (+2/+1) =1.78 eV. Likewise, In_i is a deep donor-type defect exhibiting two thermodynamic transition levels, ϵ (+3/+2) = 1.0 eV and $\varepsilon (+2/+1) = 1.37$ eV. As shown in Fig. 5, both In_i and Zn_i are donor-type defects and demonstrate considerably low formation energy under p-type conditions. In terms of anti-site defects, we found high formation energies for In_S, S_{In}, and Zn_S, which can be attributed to the significant differences in electronegativity and ionic radii between the S and Zn/In atoms. Consequently, we inferred that anion substitution for cation and vice versa is unlikely to take place in bZnIn₂S₄ and the rest of the compounds. For vacancy and interstitial defects, very similar qualitative trends are found in bZnIn2Se4 and

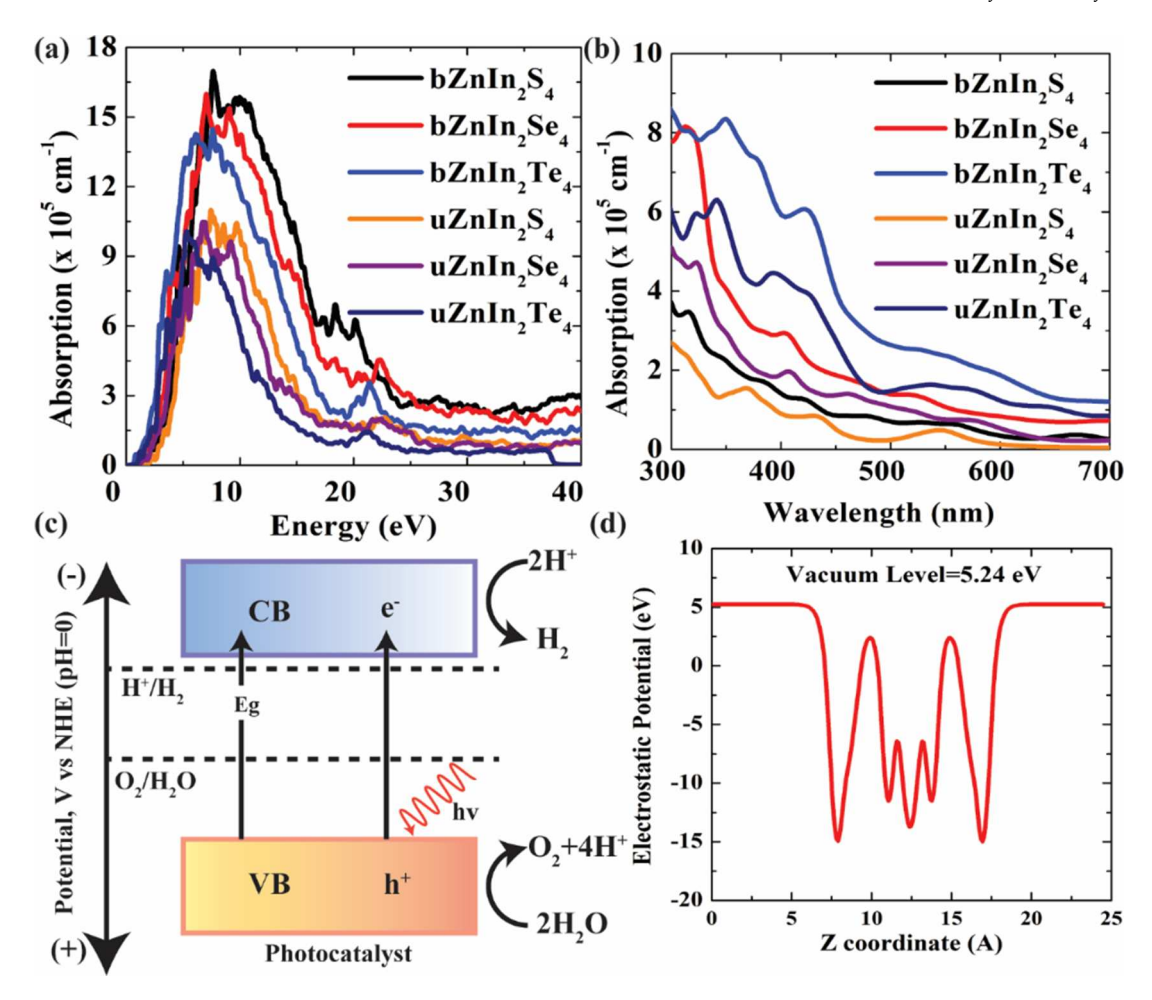


Fig. 4. Absorption coefficient as a function of (a) energy and (b) wavelength for all compounds. (c) Schematic of photocatalytic H_2O splitting. (d) Electrostatic potential with respect to vacuum for $uZnIn_2S_4$, from HSE06.

 $bZnIn_2Te_4$: V_{Zn} and V_{In} are amphoteric defects with deep levels, V_{Se} and V_{Te} have higher energies and do not form spontaneously, and Zn_i and In_i are dono-type defects with deep levels in both compounds.

The potential of an anti-site between the Zn and In atoms will be the subject of our next analysis. Although Zn_{In} may act as a shallow acceptor in $bZnIn_2S_4$ with one shallow defect level at ε (0/-1) =0.023 eV, In_{Zn} defect is a donor and does not create any transition levels in the bandgap. It is noteworthy that the formation energy of the In_{Zn} defect is significantly lower than that of the Zn_{In} defect across the E_F, whereas Zn_{In} is unstable under p-type conditions and becomes more stable under n-type conditions. This suggests that the $\mbox{In}_{\mbox{\sc Zn}}$ defect could act as a source of n-type conductivity in bZnIn₂S₄. In bZnIn₂S₄, bZnIn₂Se₄, and $bZnIn_2Te_4$, Zn_{In} and In_{Zn} are the dominant acceptor and donor type defects, respectively, and pin the equilibrium \mathbf{E}_F (evaluated using charge neutrality conditions [66]) closer to the CBE (denoted by the dotted vertical line), indicative of n-type conductivity. Zn_{In} and In_{Zn} will leave a net negative and positive charge in the system, respectively, which explains their respective acceptor and donor-type behavior. Accordingly, the synthesis of bZnIn₂S₄ under n-type growth conditions ought to result in strong electrical conductivity, and the photogenerated electrons should be able to get to the surface and engage in redox reaction without any difficulty, which might enhance the photocatalytic activity.

Turning to $uZnIn_2S_4$, it is observed that V_{Zn} could act as a donor (unlike $bZnIn_2S_4$ where it acts as an amphoteric defect) leaving only one deep transition level at ϵ (+2/0) = 0.29 eV; V_{Zn} creates a neutral defect in $uZnIn_2Se_4$ and an acceptor-type defect in $uZnIn_2Te_4$. In contrast to $bZnIn_2S_4$, V_S is stable only under p-type conditions, forming a deep level at ϵ (+2/0) = 1.50 eV, and is unstable under n-type conditions. This is in

great agreement with our recent work showing experimental and computational proof of enhanced photoreductive deuteration of carbonyls using uZnIn₂S₄ containing S vacancies [30]. The enhanced stability of V_S in ultrathin compounds can be credited to the larger surface-to-volume ratio of two-dimensional (2D) materials compared to their bulk state, which means that going from bulk to ultrathin state could drastically alter their electronic and defect properties [42]. While In creates two deep transition levels, ε (+3/+2) = 1.10 eV and ε (+2/+1)=1.44 eV, Zn_i creates only one deep level, ε (+2/+1)=1.86eV. Although Zn_{In} exhibits high formation energy under p-type conditions creating a shallow level ϵ (-1/0) = 0.08 eV and a deep level ϵ (+0/-1) = 0.80 eV, In_{Zn} is highly stable under n-type conditions and does not create any transition levels within the bandgap. Cation anti-site defects pin the equilibrium E_F closer to the CBE, indicative of n-type conductivity in uZnIn₂S₄, similar to the bulk. It should be noted that In_{Zn} and Zn_{In} are the lowest acceptors- and donor-type defects in all 6 systems, pinning the equilibrium E_F close to the CBE, leading to n-type behavior in all compounds.

It can be concluded that these metal chalcogenide photocatalysts are prone to Zn_{In} and In_{Zn} anti-site defects, and most of them could form spontaneously under certain conditions. Zn and In interstitials form slightly higher energy donor type defects with generally shallow levels. Additionally, defect energetics can vary a lot from bulk to ultrathin: e.g., in uZnIn₂S₄, V_S is stable, whereas anion vacancies are less feasible in bulk. In Fig 6, we plotted charge transition levels for some stable defects, and there are instances where certain defects become deeper as the anion changes; e.g., Zn_i ϵ (+2/+1) in bZnIn₂S₄ has been identified as shallow while it gets deeper when we move from S (\sim 0.04 eV from

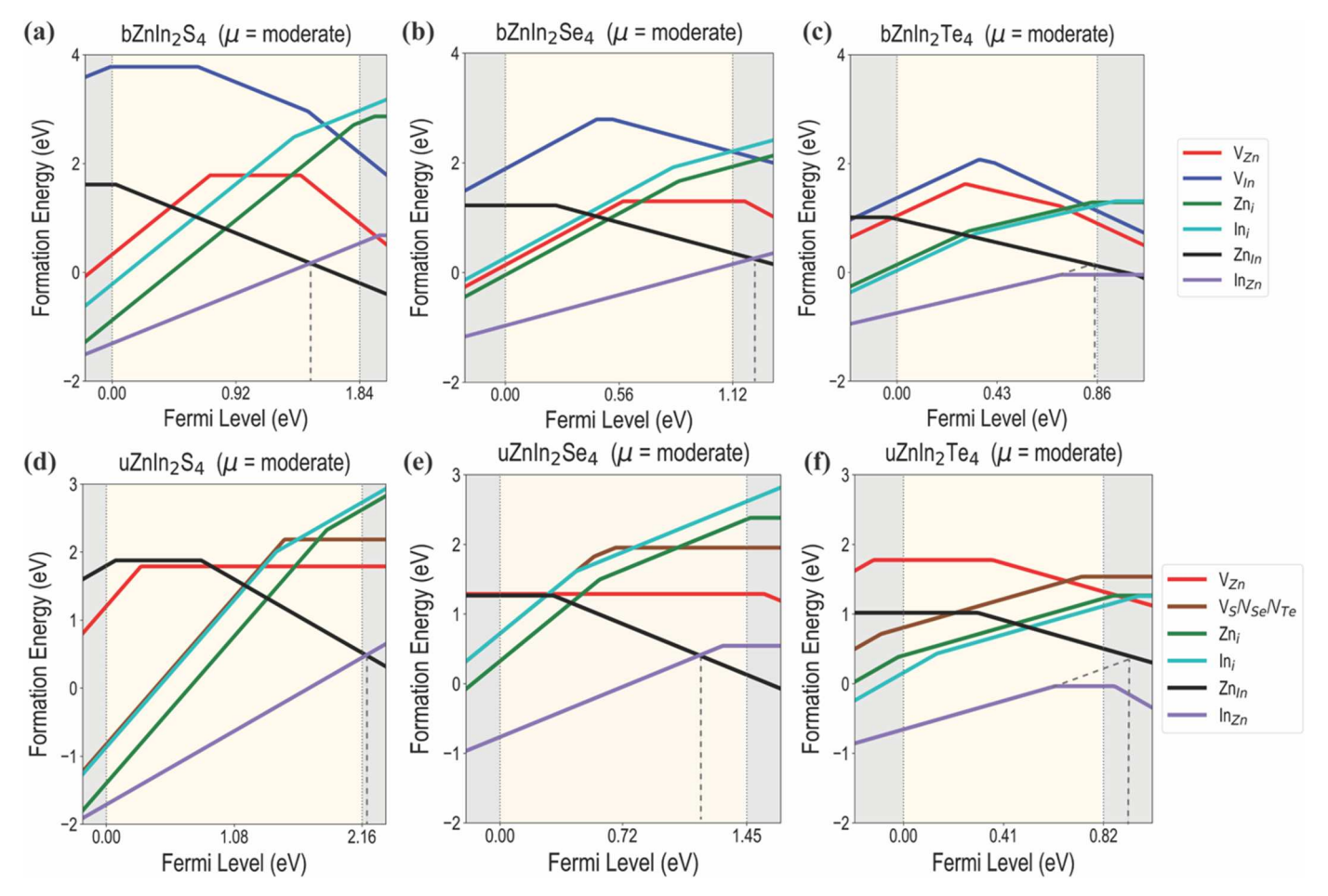


Fig. 5. The DFT-computed Fermi-level-dependent defect formation energy of selected native point defects in (a) $bZnIn_2Se_4$, (b) $bZnIn_2Se_4$, (c) $bZnIn_2Te_4$, (d) $uZnIn_2Se_4$, (e) $uZnIn_2Se_4$, and (f) $uZnIn_2Se_4$, and (f) $uZnIn_2Te_4$. All results are shown at moderate chemical potential conditions (between cation-rich and anion-rich) using GGA+U computations.

CBM) to Se (\sim 0.26 eV from CBM) to Te (\sim 0.31 eV from CBM). With the exception of $\rm In_{Zn}$, all defects create multiple energy states in the bandgap that are often deep and could alter the conductivity rendering the adsorption of species more or less favorable. We also note here that defect levels are of extreme importance while synthesizing any semiconductor, and our results can aid experiments on $\rm ZnIn_2X_4\text{-}based$ photocatalysts.

3.3. Photocatalytic hydrogen evolution reaction (HER)

In this section, we present an investigation of the photocatalytic HER on uZnIn₂X₄ surfaces with and without donor-type defects present (chosen to be Zn_i here as an example). For HER, there are typically three major steps in an acidic medium: H⁺ is first attracted to the active sites, H⁺ is then reduced by e⁻ and an adsorbed intermediate H* is created, and finally, molecular H₂ is released [97]. One of the most effective indicators of successful HER is the free energy difference $|\Delta G|$ for H adsorption. Here, $|\Delta G|$ was estimated using the equation [72]: ΔG_{HER} = $E(uZnIn_2X_4+H)-\frac{1}{2}E(H_2)-E(ZnIn_2X_4)+(\Delta ZPE-T\Delta S)$, where ZPE and ΔS were computed by considering the change in zero-point energy and entropy energy between product and reactant, respectively. The optimal value of $|\Delta G|$ for a good HER catalyst is zero. The HER suffers from a ΔG that is either excessively positive or too negative because H* cannot effectively adsorb nor desorb from the catalyst surface, respectively. We first calculated the surface energy of ultrathin compounds for varying numbers of layers or slab thickness; as seen in Table S2, we noticed a negligible effect of the surface energy on the slab thickness. Next, we considered different surface orientations (Table. S3) such as <001>, <110>, <111> and found that <001> has the lowest surface energy (which is in good agreement with other studies for surfaces in hcp crystals [73]). Following this, we considered different adsorption sites (Table. S4) such as Zn, In, S atom next to Zn or next to In, etc., and calculated $|\Delta G|$ for each, which showed that the S site next to Zn is the most favorable for H adsorption. We acknowledge that there might be other potential adsorption sites being missed here due to computational limitations.

We calculated the $|\Delta G|$ at electrode potential U=0, for defect-free uZnIn₂X₄ and found that Te-based chalcogenide exhibits the lowest free energy, followed by Se and S. The reason for this can be traced back to the lower bandgap of Te-based compounds, and higher electrical conductivity (higher E_F), compared to other compounds. Next, we introduced Zn_i defects in $uZnIn_2S_4$, $uZnIn_2Se_4$, and $uZnIn_2Te_4$, and studied how these defects may alter the photocatalytic HER. From Fig. 7(a) it is quite evident that photocatalytic activity is boosted in all compounds in the presence of the cation interstitial defect. More specifically, the calculated $|\Delta G|$ for uZnIn₂S₄, uZnIn₂Se₄, and uZnIn₂Te₄ are 1.75 eV, 1.11 eV, and 0.89 eV, whereas the computed $|\Delta G|$ for Zn_i in uZnIn₂S₄, uZnIn₂Se₄, and uZnIn₂Te₄ are 0.5 eV, 0.65 eV, and 0.60 eV, respectively. To ascertain the reason behind this, we calculated the Φ of each defectcontaining and defect-free uZnIn2X4 and found that uZnIn2X4 with a defect always exhibits lower Φ compared to pristine compounds. The higher E_F and lower Φ of defected uZnIn₂X₄ indicate higher electronic energy levels and an improved ability to provide electrons compared to that of defect-free uZnIn₂X₄ [97]. Additionally, we plotted the PDOS for Zn_i + uZnIn₂S₄, displayed in Fig 7(c), and it can be seen that some defect

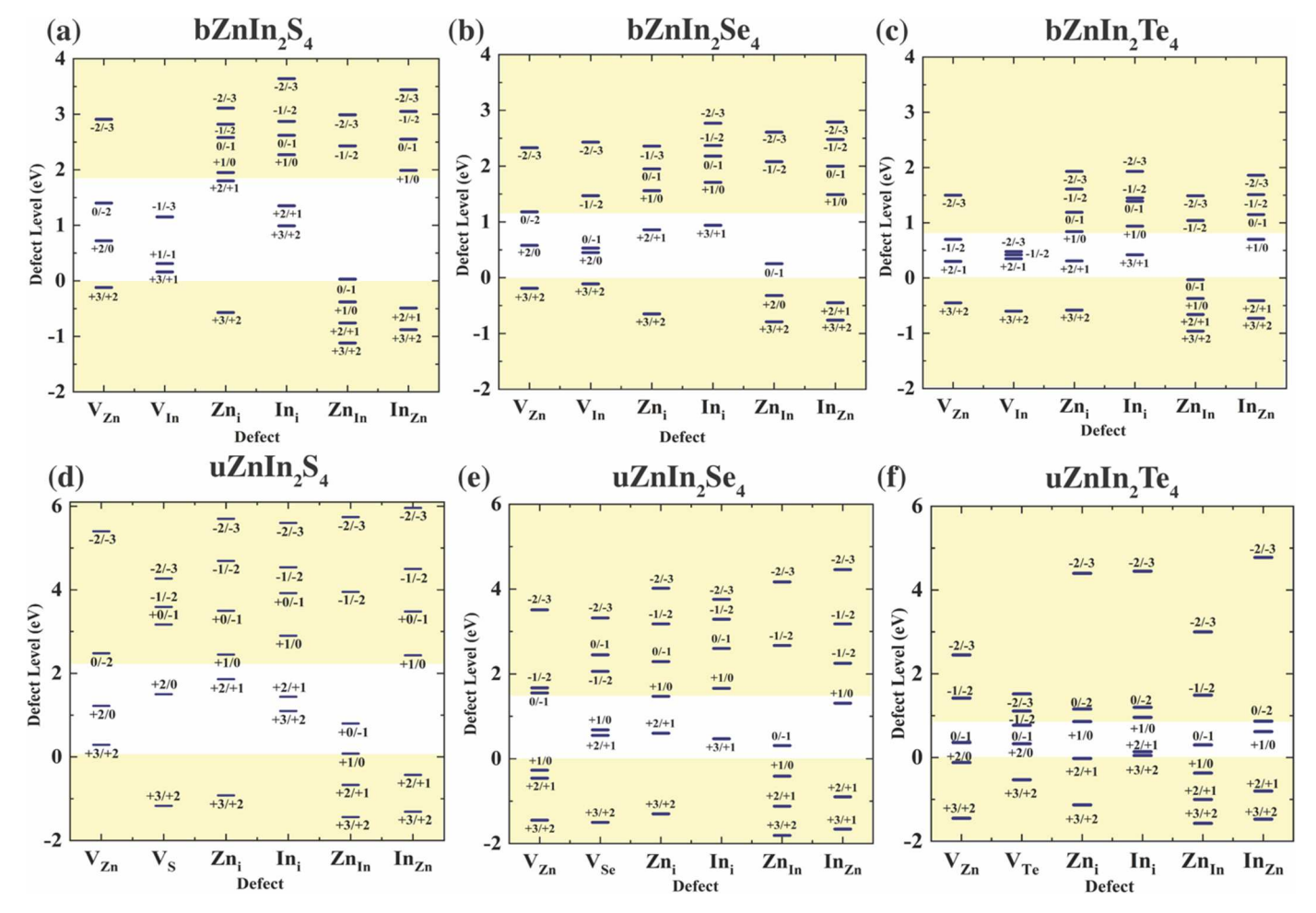


Fig. 6. DFT-computed charge transition levels of selected native point defects in (a) $bZnIn_2S_4$, (b) $bZnIn_2S_4$, (c) $bZnIn_2Te_4$, (d) $uZnIn_2S_4$, (e) $uZnIn_2S_4$, and (f) $uZnIn_2Te_4$. The white color denotes the bandgap region.

states have appeared near the E_F, which eventually provides higher electronic conductivity, therefore boosting the photocatalytic HER. For more insight into the charge transfer mechanism between the catalyst and H atom, we examined the charge density difference (CDD) between $uZnIn_2S_4$ and H, and $uZnIn_2S_4 + Zn_i$ and H, as shown in Fig 7(e-f). Zn_i creates a more electron-rich environment surrounding the adsorption site, which alters the electronic structure and bolsters conductivity. Consequently, there is more charge transfer between the catalyst and H, which results in strong adsorption. Finally, Fig 7(d) shows the computed absorption spectra of the defected uZnIn₂X₄, revealing a shift to a low-energy region compared to that of the defect-free structure. We conclude that the presence of the Zn_i defect could potentially enhance the range of visible light absorption which might promote photocatalytic reactions. We note that point defect formation energies primarily depend on the electronic structure and chemical bonding, which are relatively insensitive to temperature unless we go to very high temperatures. Therefore, the relative stability and trends of defect behavior in bZnIn₂X₄ and uZnIn₂X₄ from 0K DFT are likely to be similar at room temperature as well, although results may vary quantitatively. While the relative stability of defects is expected to hold at finite temperatures, it is important to consider the potential impact of temperature and other external factors on photocatalytic performance with defects. Additionally, the photocatalytic performance of ZnIn₂X₄ with defects may also depend on factors such as the concentration and distribution of defects, as well as other specific reaction conditions, which is beyond the scope of the current study. Consequently, further investigations of the point defects in ZnIn₂X₄ under laboratory conditions, including at elevated temperatures and under various reaction conditions, may be necessary to completely comprehend the impact of defects on photocatalytic performance. We plan to perform more AIMD simulations in the future on defect-containing $ZnIn_2X_4$ supercells to study how defect configurations change with temperature and how adsorption energies and photocatalytic performance is subsequently influenced.

3.4. Photocatalytic oxygen evolution reaction (OER)

In this section, we evaluated the impact of Zn_i in $uZnIn_2X_4$ on the photocatalytic OER, which is significantly more sophisticated than HER over the photocatalytic H_2O splitting process since it includes four-electron transfer steps [72]. The H_2O molecule is first adsorbed on the surface-active sites, accompanied by the formation of 3 different oxygenated reaction intermediates, i.e., HO^* , O^* , and HOO^* . Overall, OER reactions could be expressed as (1) $H_2O + ^* \rightarrow OH^* + H^+ + e^-$, (2) $OH^* \rightarrow O^* + H^+ + e^-$, (3) $OH^* \rightarrow OOH^* + H^+ + e^-$ and (4) $OOH^* \rightarrow OOH^* + OOH^*$, or, and OOH^* represents an active site on the bare catalyst surface, OH^* , O^* , and OOH^* represent three different oxygenated catalytic intermediates and OOH^* has been calculated for each intermediate stage using the following equations [72].

$$\Delta G_1 = E(uZnIn_2X_4 + OH) + E(H_2) - E(H_2O) - E(uZnIn_2X_4)$$
$$+ (\Delta ZPE - T\Delta S)_1 - eU$$

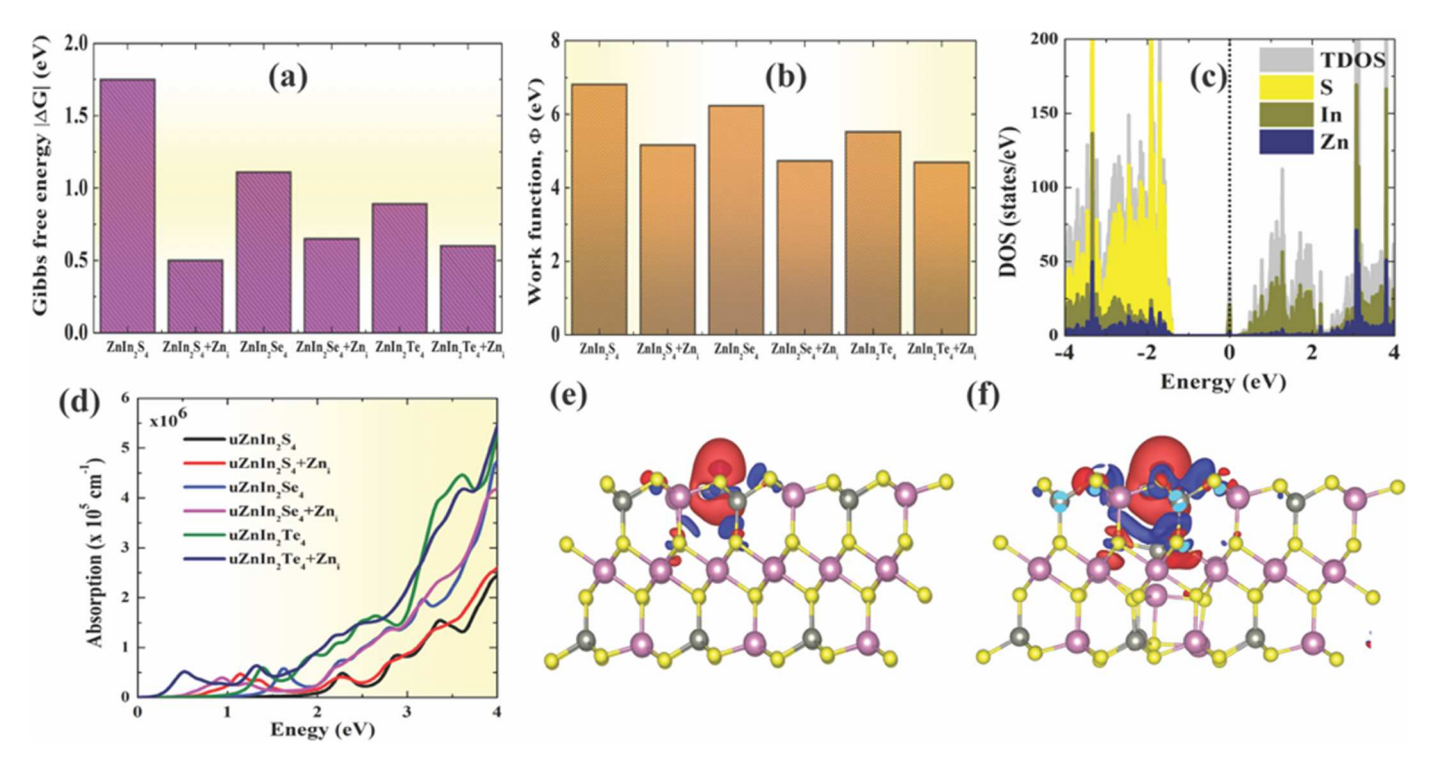


Fig. 7. (a) Gibbs free energy profile and (b) work function of multiple $ZnIn_2X_4$ compounds with and without Zn_i . (c) DOS of $uZnIn_2S_4$ containing Zn_i . (d) The absorption spectra of multiple $uZnIn_2X_4$ compounds with and without Zn_i . Charge density difference (CDD) between (e) $uZnIn_2S_4$ and H and (f) $uZnIn_2S_4 + Zn_i$ and H. Blue and red depict charge accumulation and depletion respectively. Iso surface value is set as 0.001 eÅ⁻³. (For interpretation of the references to colour in this figure legend, the reader is referred to the web version of this article.)

$$\begin{split} \Delta G_2 &= E(uZnIn_2X_4 + O) + \frac{1}{2}E(H_2) - E(uZnIn_2X_4 + OH) \\ &\quad + (\Delta ZPE - T\Delta S)_2 - eU \\ \\ \Delta G_3 &= E(uZnIn_2X_4 + OOH) + \frac{1}{2}E(H_2) - E(H_2O) - E(uZnIn_2X_4 + O) \\ &\quad + (\Delta ZPE - T\Delta S)_3 - eU \\ \\ \Delta G_4 &= 4.92 + 2E(H_2O) - 1.5E(H_2) + E(uZnIn_2X_4) - E(uZnIn_2X_4 + OOH) \\ &\quad + (\Delta ZPE - T\Delta S)_4 - eU \end{split}$$

Further, the thermodynamic overpotential can be calculated using the equation $\eta^{OER} = \frac{\max\{\Delta G_1, \Delta G_2, \Delta G_3, \Delta G_4\}}{e} - 1.23 \ V$. The OER activities of uZnIn₂X₄ are systemically analyzed using the free energy profiles of each intermediate step as depicted in Fig. 8. In general, under U=1.23 V external electrode potential, it was found that adsorption of OOH* is

relatively weak, making the third step (uphill) O* → OOH* the potential determining step. We next introduced Zn_i defects in uZnIn₂S₄, uZnIn₂Se₄, and uZnIn₂Te₄. Zn_i reduces the peak in the free energy barrier pathway $O^* \rightarrow OOH^*$ during the overall conversion of O_2 from H_2O . In particular, the thermodynamic overpotential for uZnIn₂S₄, uZnIn₂Se₄, and uZnIn2Te4 is recorded as 3.41 eV, 4.84 eV, and 3.23 eV, respectively, whereas the computed thermodynamic overpotential values for Zn_i in uZnIn₂S₄, uZnIn₂Se₄, and uZnIn₂Te₄ are 3.27 eV, 3.31 eV, and 2.91 eV, respectively. The improved OER activity in defective structures could be credited to higher E_F and lower Φ , and defect energy states within the bandgap, which eventually increase the adsorption as discussed in the previous section. We note the impact of surface coverage on HER/OER reactions has not been explicitly accounted for in this work. However, it is an important factor to consider in realistic application scenarios, as it is unlikely that the adsorbates would exist in a dilute limit. In practice, the surface coverage of the adsorbates could potentially affect the free energies and reaction barriers, which can, in

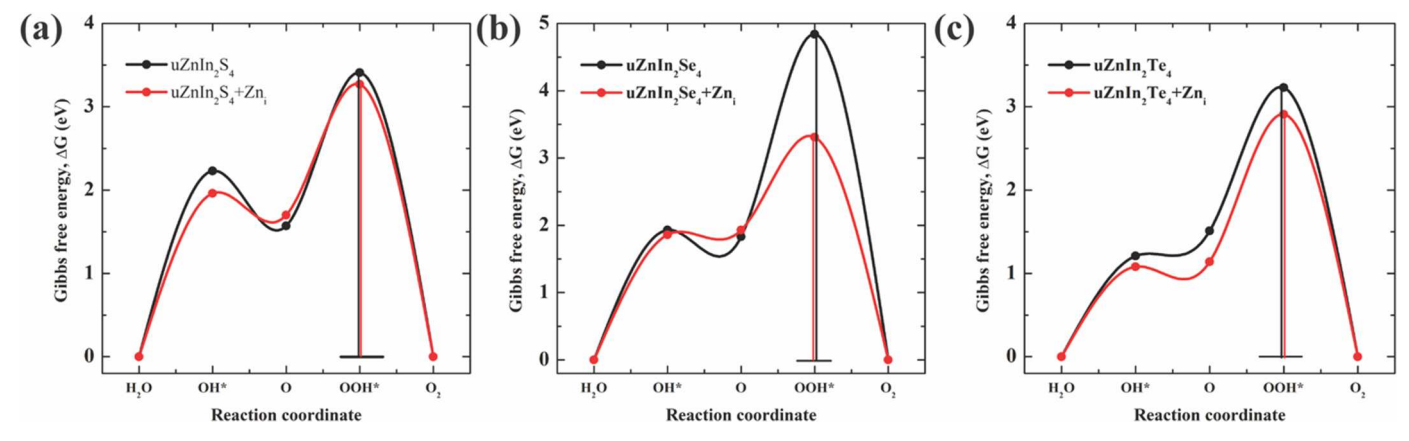


Fig. 8. The Gibbs free energy profiles of the OER pathway for (a) uZnIn₂S₄ (b) uZnIn₂Se₄ and (c) uZnIn₂Te₄ with and without defect.

turn, affect the catalytic activity. Therefore, to fully understand the impact of surface coverage on HER/OER reactions, it would be necessary to perform a series of simulations with varying concentrations of adsorbates on the surface. Eventually, this would allow us to determine the coverage-dependent changes in the electronic level and thermodynamic properties of the material, as well as the resulting changes in the catalytic activity. Although this level of detail is beyond the scope of our current work, undoubtedly it might be an important consideration for future computational studies of $uZnIn_2X_4$ and related materials.

Conclusions

In this work, first principles computations were used to study point defects in bulk and ultrathin $ZnIn_2X_4$ compounds, where X = S, Se, or Te. We first studied the structural stability and optoelectronic properties of bZnIn₂X₄ and uZnIn₂X₄. GGA+U calculations showed that from S to Se to Te, lattice constants and absorption coefficients increase, while the electronic bandgap reduces. From bulk to ultrathin compounds, the electronic bandgap increases while the absorption coefficients go down. Importantly, uZnIn₂S₄ holds great promise for photocatalytic water splitting as it exhibits sufficient overpotential for oxidation and reduction reactions based on HSE06 calculations. We simulated all possible native defects and identified the lowest energy acceptor/donor as well as shallow/deep level defects considering different growth conditions, namely In-rich, X-rich, and moderate conditions. DFT data suggest that in moderate chemical potential growth conditions, the Zn_{In} and In_{Zn} are the dominant acceptors and donor defects, respectively, and they could be the source of n-type conductivity in these metal chalcogenide photocatalysts as they pin the equilibrium E_F closer to the electron-rich edge. Additionally, it has been realized that defect energetics in the bulk state and ultrathin state are quite different, such as in uZnIn₂S₄. where V_S turns out to be a stable defect, unlike the bulk. Furthermore, most of these native defects yield multiple energy states in the bandgap that are often deep, which could potentially affect the adsorption of molecules. The photocatalytic HER on the surface of uZnIn₂X₄ was studied, showing that uZnIn2Te4 holds great promise for efficient HER, followed by uZnIn₂Se₄ and uZnIn₂S₄. Additionally, our computations suggest that metal interstitial defects could make the adsorption and desorption of H more energetically favorable which in turn promotes the HER. The impact of metal interstitials on the photocatalytic OER process was also studied, revealing that they could potentially reduce the free energy barrier of OER pathways as endorsed by reduced thermodynamic overpotential.

Declaration of Competing Interest

The authors declare that they have no known competing financial interests or personal relationships that could have appeared to influence the work reported in this paper.

Data availability

Data that supports the finding of this study is already added to the manuscript.

Acknowledgment

A. M. K. acknowledges funding from the National Science Foundation (CHE-1955358) and computational resources on the Rosen Center for Advanced Computing (RCAC) clusters at Purdue and the Laboratory Computing Resource Center (LCRC) at Argonne National Laboratory. Y. S. acknowledges the support of the National Science Foundation (CHE-1955358), the Herman Frasch Foundation (820-HF17), and the University of Cincinnati. A.M.K. also acknowledges support from the School of Materials Engineering at Purdue University under Account No.

F.10023800.05.002.

References

- U. Alam, A. Khan, W. Raza, A. Khan, D. Bahnemann, M. Muneer, Highly efficient Y and V co-doped ZnO photocatalyst with enhanced dye sensitized visible light photocatalytic activity, Catal. Today 284 (2017) 169–178, https://doi.org/10.1016/J.CATTOD.2016.11.037.
- [2] X. Chang, G. Yu, J. Huang, Z. Li, S. Zhu, P. Yu, C. Cheng, S. Deng, G. Ji, Enhancement of photocatalytic activity over NaBiO3/BiOCl composite prepared by an *in situ* formation strategy, Catal. Today 153 (2010) 193–199, https://doi.org/ 10.1016/J.CATTOD.2010.02.069.
- [3] R. Daghrir, P. Drogui, D. Robert, Modified TiO2 for environmental photocatalytic applications: a review, Ind. Eng. Chem. Res. 52 (2013) 3581–3599. https://pubs. acs.org/doi/abs/10.1021/ie303468t, accessed November 22, 2021.
- [4] U. Alam, M. Fleisch, I. Kretschmer, D. Bahnemann, M. Muneer, One-step hydrothermal synthesis of Bi-TiO2 nanotube/graphene composites: An efficient photocatalyst for spectacular degradation of organic pollutants under visible light irradiation, Appl. Catal. B 218 (2017) 758–769, https://doi.org/10.1016/J. APCATB.2017.06.016.
- [5] X. Shi, L. Mao, P. Yang, H. Zheng, M. Fujitsuka, J. Zhang, T. Majima, Ultrathin ZnIn2S4 nanosheets with active (110) facet exposure and efficient charge separation for cocatalyst free photocatalytic hydrogen evolution, Appl. Catal. B 265 (2020), 118616. https://doi.org/10.1016/j.apcatb.2020.118616.
- [6] G. Zhang, H. Wu, D. Chen, N. Li, Q. Xu, H. Li, J. He, J. Lu, A mini-review on ZnIn2S4-Based photocatalysts for energy and environmental application, Green Energy and Environment 7 (2022) 176–204, https://doi.org/10.1016/j. gee 2020 12 015
- [7] J. Wang, S. Sun, R. Zhou, Y. Li, Z. He, H. Ding, D. Chen, W. Ao, A review: Synthesis, modification and photocatalytic applications of ZnIn2S4, J. Mater. Sci. Technol. 78 (2021) 1–19, https://doi.org/10.1016/j.jmst.2020.09.045.
- [8] A. Fujishima, K. Honda, Electrochemical Photolysis of Water at a Semiconductor Electrode, Nature 1972 238 5358 (238) (1972) 37–38, https://doi.org/10.1038/ 238037a0.
- [9] X. Zhou, J. Shi, C. Li, Effect of Metal Doping on Electronic Structure and Visible Light Absorption of SrTiO 3 and NaTaO 3 (Metal = Mn, Fe, and Co) 3 (2011) 8305–8311
- [10] G. Han, G. Li, J. Huang, C. Han, C. Turro, Y. Sun, Two-photon-absorbing ruthenium complexes enable near infrared light-driven photocatalysis, Nature Communications 2022 13 13 (1) (2022) 1–10, https://doi.org/10.1038/s41467-022-29981-3.
- [11] F. Song, T. Zhang, D. Zhou, P. Sun, Z. Lu, H. Bian, J. Dang, H. Gao, Y. Qian, W. Li, N. Jiang, H. Dummer, J.G. Shaw, S. Chen, G. Chen, Y. Sun, Y. Rao, Charge Transfer of Interfacial Catalysts for Hydrogen Energy, ACS Mater Lett 4 (2022) 967–977, https://doi.org/10.1021/ACSMATERIALSLETT.2C00143/ASSET/IMAGES/ LARGE/TZ2C00143 0006_JPEG.
- [12] L. Du, Y. Sun, B. You, Hybrid water electrolysis: Replacing oxygen evolution reaction for energy-efficient hydrogen production and beyond, Materials Reports: Energy 1 (2021), 100004, https://doi.org/10.1016/J.MATRE.2020.12.001.
- [13] G. Han, X. Liu, Z. Cao, Y. Sun, Photocatalytic pinacol C-C coupling and jet fuel precursor production on ZnIn2S4nanosheets, ACS Catal 10 (2020) 9346–9355, https://doi.org/10.1021/ACSCATAL.0C01715/ASSET/IMAGES/LARGE/ CS0C01715 0008_JPEG.
- [14] Ü. Özgür, Y.I. Alivov, C. Liu, A. Teke, M.A. Reshchikov, S. Doğan, V. Avrutin, S. J. Cho, H. Morko, A comprehensive review of ZnO materials and devices, J. Appl. Phys. 98 (2005), https://doi.org/10.1063/1.1992666.
- [15] X. Cao, B. Zheng, X. Rui, W. Shi, Q. Yan, H. Zhang, Metal oxide-coated three-dimensional graphene prepared by the use of metal-organic frameworks as precursors, Angewandte Chemie International Edition 53 (2014) 1404–1409, https://doi.org/10.1002/ANIE.201308013.
- [16] F.E. Osterloh, Inorganic nanostructures for photoelectrochemical and photocatalytic water splitting, Chem. Soc. Rev. 42 (2013) 2294–2320, https://doi. org/10.1039/C2CS35266D.
- [17] A. Wibowo, M.A. Marsudi, M.I. Amal, M.B. Ananda, R. Stephanie, H. Ardy, L. J. Diguna, ZnO nanostructured materials for emerging solar cell applications, RSC Adv. 10 (2020) 42838–42859, https://doi.org/10.1039/D0RA07689A.
- [18] J. Low, B. Cheng, J. Yu, Surface modification and enhanced photocatalytic CO2 reduction performance of TiO2: a review, Appl. Surf. Sci. 392 (2017) 658–686, https://doi.org/10.1016/J.APSUSC.2016.09.093.
- [19] D. Maarisetty, S.S. Baral, Defect engineering in photocatalysis: formation, chemistry, optoelectronics, and interface studies, J. Mater. Chem. A Mater. 8 (2020) 18560–18604, https://doi.org/10.1039/d0ta04297h.
- [20] C. Du, Q. Zhang, Z. Lin, B. Yan, C. Xia, G. Yang, Half-unit-cell ZnIn2S4 monolayer with sulfur vacancies for photocatalytic hydrogen evolution, Appl. Catal. B 248 (2019) 193–201, https://doi.org/10.1016/j.apcatb.2019.02.027.
- [21] Y.J. Zhang, H.M. Tang, S.P. Gao, Density functional theory study of ZnIn2S4 and CdIn2S4 polymorphs using full-potential linearized augmented plane wave method and modified becke–Johnson potential, Phys. Status Solidi B Basic Res. 257 (2020) 1–10, https://doi.org/10.1002/pssb.201900485.
- [22] Z. Zafar, S. Yi, J. Li, C. Li, Y. Zhu, A. Zada, W. Yao, Z. Liu, X. Yue, Recent development in defects engineered photocatalysts: an overview of the experimental and theoretical strategies, Energy Environ. Mater. 5 (2022) 68–114, https://doi.org/10.1002/eem2.12171.
- [23] W.K. Chong, B.J. Ng, C.C. Er, L.L. Tan, S.P. Chai, Insights from density functional theory calculations on heteroatom P-doped ZnIn2S4 bilayer nanosheets with

- atomic-level charge steering for photocatalytic water splitting, Sci. Rep. 12 (2022) 1-11, https://doi.org/10.1038/s41598-022-05740-8.
- [24] P. Wang, Z. Shen, Y. Xia, H. Wang, L. Zheng, W. Xi, S. Zhan, Atomic insights for optimum and excess doping in photocatalysis: a case study of few-layer Cu-ZnIn2S4, Adv. Funct. Mater. 29 (2019) 1–9, https://doi.org/10.1002/ adfm 201807013
- [25] J. Chen, F. Xin, X. Yin, T. Xiang, Y. Wang, Synthesis of hexagonal and cubic ZnIn2S4 nanosheets for the photocatalytic reduction of CO2 with methanol, RSC Adv. 5 (2015) 3833–3839, https://doi.org/10.1039/c4ra13191f.
- [26] Z. Lei, W. You, M. Liu, G. Zhou, T. Takata, M. Hara, K. Domen, C. Li, Photocatalytic water reduction under visible light on a novel ZnIn2S4 catalyst synthesized by hydrothermal method, Chem. Commun. (2003) 2142–2143, https://doi.org/ 10.1039/B306813G.
- [27] Y. Chen, S. Hu, W. Liu, X. Chen, L. Wu, X. Wang, P. Liu, Z. Li, Controlled syntheses of cubic and hexagonal ZnIn2S4 nanostructures with different visible-light photocatalytic performance, Dalton Trans. 40 (2011) 2607–2613, https://doi.org/ 10.1039/C0DT01435D.
- [28] J. Wang, Y. Chen, W. Zhou, G. Tian, Y. Xiao, H.H. Fu, H.H. Fu, Cubic quantum dot/hexagonal microsphere Znln2S4 heterophase junctions for exceptional visible-light-driven photocatalytic H2 evolution, J. Mater. Chem. A Mater. 5 (2017) 8451–8460, https://doi.org/10.1039/C7TA01914A.
- [29] Y. Chen, R. Huang, D. Chen, Y. Wang, W. Liu, X. Li, Z. Li, Exploring the different photocatalytic performance for dye degradations over hexagonal ZnIn 2S 4 microspheres and cubic ZnIn 2S 4 nanoparticles, ACS Appl. Mater. Interfaces 4 (2012) 2273–2279, https://doi.org/10.1021/AM300272F/SUPPL_FILE/ AM300272F SI 001.PDF.
- [30] C. Han, G. Han, S. Yao, L. Yuan, X. Liu, Z. Cao, A. Mannodi-Kanakkithodi, Y. Sun, Defective ultrathin ZnIn2S4 for photoreductive deuteration of carbonyls using D2O as the deuterium source, Adv. Sci. 9 (2022) 1–10, https://doi.org/10.1002/ advs.202103408
- [31] A.R. Gunjal, A.R. Gunjal, A.K. Kulkarni, U.v. Kawade, Y.A. Sethi, R.S. Sonawane, J. Ook-Baeg, A.v. Nagawade, B.B. Kale, A hierarchical SnS@ZnIn2S4 marigold flower-like 2D nano-heterostructure as an efficient photocatalyst for sunlight-driven hydrogen generation, Nanoscale Adv. 2 (2020) 2577–2586, https://doi.org/10.1039/D0NA00175A
- [32] Y. Chen, G. Tian, W. Zhou, Y. Xiao, J. Wang, X. Zhang, H. Fu, Enhanced photogenerated carrier separation in CdS quantum dot sensitized ZnFe2O4/ ZnIn2S4 nanosheet stereoscopic films for exceptional visible light photocatalytic H2 evolution performance, Nanoscale 9 (2017) 5912–5921, https://doi.org/ 10.1039/C7NR00155J.
- [33] S. Chen, F. Xie, X. Wang, X. Zhao, Z. Tang, Efficient charge separation between ZnIn2S4 nanoparticles and polyaniline nanorods for nitrogen photofixation, New J. Chem. 44 (2020) 7350–7356, https://doi.org/10.1039/D0NJ01102A.
- [34] Z. Li, X. Wang, W. Tian, A. Meng, L. Yang, CoNi bimetal cocatalyst modifying a hierarchical ZnIn2S4 nanosheet-based microsphere noble-metal-free photocatalyst for efficient visible-light-driven photocatalytic hydrogen production, ACS Sustain. Chem. Eng. 7 (2019) 20190–20201, https://doi.org/10.1021/ ACSSUSCHEMENG.9806430/SUPPL.FILE/SC9806430 St 001.PDF.
- [35] J. Chen, K. Li, X. Cai, Y. Zhao, X. Gi, L. Mao, Sulfur vacancy-rich ZnIn2S4 nanosheet arrays for visible-light-driven water splitting, Mater. Sci. Semicond. Process. 143 (2022), 106547, https://doi.org/10.1016/J.MSSP.2022.106547.
- [36] F. Tian, R. Zhu, K. Song, F. Ouyang, G. Cao, The effects of amount of La on the photocatalytic performance of ZnIn2S4 for hydrogen generation under visible light, Int. J. Hydrog. Energy 40 (2015) 2141–2148, https://doi.org/10.1016/J. LIHYDENE 2014 12 025
- [37] F. Tian, R. Zhu, Y. He, F. Ouyang, Improving photocatalytic activity for hydrogen evolution over ZnIn2S4 under visible-light: A case study of rare earth modification, Int. J. Hydrog. Energy 39 (2014) 6335–6344, https://doi.org/10.1016/J. JJHYDENE.2014.01.188.
- [38] C. Tan, G. Zhu, M. Hojamberdiev, K.S. Lokesh, X. Luo, L. Jin, J. Zhou, P. Liu, Adsorption and enhanced photocatalytic activity of the {0 0 0 1} faceted Sm-doped ZnIn2S4 microspheres, J. Hazard. Mater. 278 (2014) 572–583, https://doi.org/ 10.1016/J.JHAZMAT.2014.06.019.
- [39] Y. Wang, D. Chen, L. Qin, J. Liang, Y. Huang, Hydrogenated ZnIn2S4 microspheres: boosting photocatalytic hydrogen evolution by sulfur vacancy engineering and mechanism insight, Phys. Chem. Chem. Phys. 21 (2019) 25484–25494, https://doi. org/10.1039/C9CP04709C.
- [40] S. Sukharom, A. Boonchun, P. Reunchan, S. Jungthawan, S. Limpijumnong, J. T-Thienprasert, Effect of native point defects on the photocatalytic performance of ZnIn2S4, Phys. B Condens. Matter 630 (2022), 413674, https://doi.org/10.1016/J. PHYSB.2022.413674.
- [41] H.J. Queisser, E.E. Haller, Defects in semiconductors: Some fatal, some vital, Science 281 (1998) (1979) 945–950, https://doi.org/10.1126/ SCIENCE 281-523 0.45
- [42] D. Wang, X. bin Li, D. Han, W.Q. Tian, H.B. Sun, Engineering two-dimensional electronics by semiconductor defects, Nano Today 16 (2017) 30–45, https://doi. org/10.1016/J.NANTOD.2017.07.001.
- [43] D. Lee, J.W. Park, N.K. Cho, J. Lee, Y.S. Kim, Verification of charge transfer in metal-insulator-oxide semiconductor diodes via defect engineering of insulator, Sci. Rep. 9 (9) (2019) 1–9, https://doi.org/10.1038/s41598-019-46752-1, 20191.
- [44] Y.N. Teja, R.M. Prakash, A. Murali, M. Sakar. Chapter 5 Defective photocatalysts, Photocatalytic Systems by Design, Materials, Mechanisms and Applications, 2021, pp. 131–163, https://doi.org/10.1016/B978-0-12-820532-7.00006-0.
- [45] M. Kumar, P. Basera, S. Saini, S. Bhattacharya, Role of defects in photocatalytic water splitting: monodoped vs codoped SrTiO3, J. Phys. Chem. C 124 (2020)

- 10272-10279, https://doi.org/10.1021/ACS.JPCC.9B11160/SUPPL_FILE/JP9B11160 SI 001.PDF.
- [46] X. Jiao, Z. Chen, X. Li, Y. Sun, S. Gao, W. Yan, C. Wang, Q. Zhang, Y. Lin, Y. Luo, Y. Xie, Defect-mediated electron-hole separation in one-unit-cell ZnIn2S4 layers for boosted solar-driven CO2 reduction, J. Am. Chem. Soc. 139 (2017) 7586–7594, https://doi.org/10.1021/JACS.7B02290/SUPPL_FILE/JA7B02290_SI_001.PDF.
- [47] X. Jing, N. Lu, J. Huang, P. Zhang, Z. Zhang, One-step hydrothermal synthesis of S-defect-controlled ZnIn2S4 microflowers with improved kinetics process of charge-carriers for photocatalytic H2 evolution, J.Energy Chem. 58 (2021) 397–407, https://doi.org/10.1016/J.JECHEM.2020.10.032.
- [48] C. Foo, Y. Li, K. Lebedev, T. Chen, S. Day, C. Tang, S.C.E. Tsang, Characterisation of oxygen defects and nitrogen impurities in TiO2 photocatalysts using variable-temperature X-ray powder diffraction, Nat. Commun. 1 (12) (2021) 1–13, https://doi.org/10.1038/s41467-021-20977-z. 2021 12.
- [49] F.G. Sen, A. Mannodi-Kanakkithodi, T. Paulauskas, J. Guo, L. Wang, A. Rockett, M. J. Kim, R.F. Klie, M.K.Y. Chan, Computational design of passivants for CdTe grain boundaries, Sol. Energy Mater. Sol. Cells 232 (2021), 111279, https://doi.org/10.1016/J.SOLMAT.2021.111279.
- [50] A. Mannodi-Kanakkithodi, J.S. Park, A.B.F. Martinson, M.K.Y. Chan, Defect energetics in pseudo-cubic mixed halide lead perovskites from first-principles, J. Phys. Chem. C 124 (2020) 16729–16738, https://doi.org/10.1021/acs. incc.0r02486.
- [51] A. Mannodi-Kanakkithodi, J.S. Park, N. Jeon, D.H. Cao, D.J. Gosztola, A.B. F. Martinson, M.K.Y. Chan, Comprehensive computational study of partial lead substitution in methylammonium lead bromide, Chem. Mater. (2019), https://doi.org/10.1021/acs.chemmater.8b04017.
- [52] A. Mannodi-Kanakkithodi, M.Y. Toriyama, F.G. Sen, M.J. Davis, R.F. Klie, M.K. Y. Chan, Machine-learned impurity level prediction for semiconductors: the example of Cd-based chalcogenides, NPJ Comput. Mater. 6 (2020) 1–14, https://doi.org/10.1038/s41524-020-0296-7.
- [53] A. Luque, A. Martí, C. Stanley, Understanding intermediate-band solar cells, Nat. Photonics 3 (6) (2012) 146–152, https://doi.org/10.1038/nphoton.2012.1, 2012
- [54] A. Luque, A. Martí, Increasing the efficiency of ideal solar cells by photon induced transitions at intermediate levels, Phys. Rev. Lett. 78 (5014) (1997), https://doi. org/10.1103/PhysRevLett.78.5014.
- [55] A. Martí, E. Antolín, C.R. Stanley, C.D. Farmer, N. López, P. Díaz, E. Cánovas, P. G. Linares, A. Luque, Production of photocurrent due to intermediate-to-conduction-band transitions: A demonstration of a key operating principle of the intermediate-band solar cell, Phys. Rev. Lett. 97 (2006), 247701, https://doi.org/10.1103/PHYSREVLETT.97.247701/FIGURES/5/MEDIUM.
- [56] I. Aguilera, P. Palacios, P. Wahnón, Understanding Ti intermediate-band formation in partially inverse thiospinel MgIn2S4 through many-body approaches, Phys Rev B Condens Matter Mater Phys 84 (2011), 115106, https://doi.org/10.1103/ PHYSREVB.84.115106/FIGURES/4/MEDIUM.
- [57] S. Sonoda, Partially filled intermediate band of Cr-doped GaN films, Appl. Phys. Lett. 100 (2012), 202101, https://doi.org/10.1063/1.4717716.
- [58] C. Yang, M. Qin, Y. Wang, D. Wan, F. Huang, J. Lin, Observation of an intermediate band in Sn-doped chalcopyrites with wide-spectrum solar response, Sci. Rep. 3 (3) (2013) 1–7, https://doi.org/10.1038/srep01286, 20131.
- [59] J.T. Sullivan, C.B. Simmons, J.J. Krich, A.J. Akey, D. Recht, M.J. Aziz, T. Buonassisi, Methodology for vetting heavily doped semiconductors for intermediate band photovoltaics: a case study in sulfur-hyperdoped silicon, J. Appl. Phys. 114 (2013), 103701, https://doi.org/10.1063/1.4820454.
- [60] S.P. Bremner, M.Y. Levy, C.B. Honsberg, Limiting efficiency of an intermediate band solar cell under a terrestrial spectrum, Appl. Phys. Lett. 92 (2008), 171110, https://doi.org/10.1063/1.2907493.
- [61] Y. Okada, N.J. Ekins-Daukes, T. Kita, R. Tamaki, M. Yoshida, A. Pusch, O. Hess, C. C. Phillips, D.J. Farrell, K. Yoshida, N. Ahsan, Y. Shoji, T. Sogabe, J.F. Guillemoles, Intermediate band solar cells: recent progress and future directions, Appl. Phys. Rev. 2 (2015), 021302, https://doi.org/10.1063/1.4916561.
- Rev. 2 (2015), 021302, https://doi.org/10.1063/1.4916561.
 [62] M. Rasukkannu, D. Velauthapillai, P. Vajeeston, A first-principle study of the electronic, mechanical and optical properties of inorganic perovskite Cs2SnI6 for intermediate-band solar cells, Mater. Lett. 218 (2018) 233–236, https://doi.org/10.1016/J.MATLET.2018.02.034.
- [63] Y. Chao, P. Zhou, N. Li, J. Lai, Y. Yang, Y. Zhang, Y. Tang, W. Yang, Y. Du, D. Su, Y. Tan, S. Guo, Ultrathin visible-light-driven mo incorporating In2O3–ZnIn2Se4 Z-scheme nanosheet photocatalysts, Adv. Mater. 31 (2019), 1807226, https://doi.org/10.1002/ADMA.201807226.
- [64] C. Tan, X. Cao, X.J. Wu, Q. He, J. Yang, X. Zhang, J. Chen, W. Zhao, S. Han, G. H. Nam, M. Sindoro, H. Zhang, Recent advances in ultrathin two-dimensional nanomaterials, Chem. Rev. 117 (2017) 6225–6331, https://doi.org/10.1021/ACS.CHEMREV.6B00558/ASSET/IMAGES/LARGE/CR-2016-00558Y_0045.JPEG.
- [65] A. Mannodi-Kanakkithodi, M.K.Y. Chan, Accelerated screening of functional atomic impurities in halide perovskites using high-throughput computations and machine learning, J. Mater. Sci. 2022 (2022) 1–19, https://doi.org/10.1007/ \$10853-022-0698-7
- [66] A. Mannodi-Kanakkithodi, X. Xiang, L. Jacoby, R. Biegaj, S.T. Dunham, D. R. Gamelin, M.K.Y. Chan, Universal machine learning framework for defect predictions in zinc blende semiconductors, Patterns (2022), 100450, https://doi.org/10.1016/J.PATTER.2022.100450.
- [67] J.L. Lyons, C.G. van de Walle, Computationally predicted energies and properties of defects in GaN, NPJ Comput. Mater. 3 (2017) 1–9, https://doi.org/10.1038/ s41524-017-0014-2.

- [68] G. Kresse, J. Furthmüller, Efficient iterative schemes for ab initio total-energy calculations using a plane-wave basis set, Phys. Rev. B 54 (1996) 11169, https://doi.org/10.1103/PhysRevB.54.11169.
- [69] P.E. Blöchl, Projector augmented-wave method, Phys. Rev. B 50 (1994) 17953, https://doi.org/10.1103/PhysRevB.50.17953.
- [70] J.P. Perdew, K. Burke, M. Ernzerhof, Generalized gradient approximation made simple, Phys. Rev. Lett. 77 (1996) 3865, https://doi.org/10.1103/ Phys. Phys. July 17, 3865.
- [71] J. Wang, Z. Luo, X. Zhang, X. Zhang, J. Shi, T. Cao, X. Fan, Single transition metal atom anchored on VSe2 as electrocatalyst for nitrogen reduction reaction, Appl. Surf. Sci. 580 (2022), 152272, https://doi.org/10.1016/J.APSUSC.2021.152272.
- [72] Z. Xue, X. Zhang, J. Qin, R. Liu, Constructing MoS2/g-C3N4 heterojunction with enhanced oxygen evolution reaction activity: A theoretical insight, Appl. Surf. Sci. 510 (2020), 145489, https://doi.org/10.1016/j.apsusc.2020.145489.
- [73] J.M. Zhang, D.D. Wang, K.W. Xu, Calculation of the surface energy of hcp metals by using the modified embedded atom method, Appl. Surf. Sci. 253 (2006) 2018–2024, https://doi.org/10.1016/J.APSUSC.2006.03.080.
- [74] T. Jing, D. Liang, J. Hao, M. Deng, S. Cai, Single Pt atoms stabilized on Mo2TiC2O2 for hydrogen evolution: A first-principles investigation, J. Chem. Phys. (2019) 151, https://doi.org/10.1063/1.5099571.
- [75] J. Islam, A.K.M.A. Hossain, Semiconducting to metallic transition with outstanding optoelectronic properties of CsSnCl 3 perovskite under pressure, Sci. Rep. 1 (10) (2020) 1–11, https://doi.org/10.1038/s41598-020-71223-3, 2020 10.
- [76] C. Freysoldt, B. Grabowski, T. Hickel, J. Neugebauer, G. Kresse, A. Janotti, C.G. van de Walle, First-principles calculations for point defects in solids, Rev. Mod. Phys. 86 (2014) 253–305, https://doi.org/10.1103/REVMODPHYS.86.253/FIGURES/ 24/MEDIUM.
- [77] R. González, W. López-Pérez, Á. González-García, M.G. Moreno-Armenta, R. González-Hernández, Vacancy charged defects in two-dimensional GaN, Appl. Surf. Sci. 433 (2018) 1049–1055, https://doi.org/10.1016/j.apsusc.2017.10.136.
- [78] S. Hong, S. Tiwari, A. Krishnamoorthy, K.I. Nomura, C. Sheng, R.K. Kalia, A. Nakano, F. Shimojo, P. Vashishta, Sulfurization of MoO3in the chemical vapor deposition synthesis of MoS2enhanced by an H2S/H2mixture, J. Phys. Chem. Lett. 12 (2021) 1997–2003, https://doi.org/10.1021/ACS.JPCLETT.0C03280/SUPPL_ FILE/JZ0C03280_SI_001.PDF.
- [79] E.M. Flores, M.L. Moreira, M.J. Piotrowski, ZnF2, and ZnO/ZnF2: A DFT investigation within PBE, PBE + U, and hybrid HSE functionals, J. Phys. Chem. A 124 (2020) 3778–3785, https://doi.org/10.1021/ACS.JPCA.9B11415/SUPPL_FILE.JJP9B11415 SI 001.PDF.
- [80] J. Gusakova, X. Wang, L.L. Shiau, A. Krivosheeva, V. Shaposhnikov, V. Borisenko, V. Gusakov, B.K. Tay, Electronic properties of bulk and monolayer TMDs: theoretical study within DFT framework (GVJ-2e Method), Phys. Status Solidi 214 (2017), 1700218, https://doi.org/10.1002/PSSA.201700218.
- [81] C.R. Ryder, J.D. Wood, S.A. Wells, M.C. Hersam, Chemically tailoring semiconducting two-dimensional transition metal dichalcogenides and black phosphorus, ACS Nano 10 (2016) 3900–3917, https://doi.org/10.1021/ acsnano.6b01091.
- [82] N. Lu, H. Guo, L. Li, J. Dai, L. Wang, W.N. Mei, X. Wu, X.C. Zeng, MoS2/MX2 heterobilayers: bandgap engineering via tensile strain or external electrical field, Nanoscale 6 (2014) 2879–2886, https://doi.org/10.1039/C3NR06072A.
- [83] A. Chaves, J.G. Azadani, H. Alsalman, D.R. da Costa, R. Frisenda, A.J. Chaves, S.H. Song, Y.D. Kim, D. He, J. Zhou, A. Castellanos-Gomez, F.M. Peeters, Z. Liu, C.L. Hinkle, S.H. Oh, P.D. Ye, S.J. Koester, Y.H. Lee, P. Avouris, X. Wang, T. Low, Bandgap engineering of two-dimensional semiconductor materials, NPJ 2D Mater. Appl. 2020 4:1. 4 (2020) 1–21. 10.1038/s41699-020-00162-4.

- [84] M.A. Mohebpour, B. Mortazavi, T. Rabczuk, X. Zhuang, A.v. Shapeev, M.B. Tagani, Mechanical, optical, and thermoelectric properties of semiconducting ZnIn2X4 (X= S, Se, Te) monolayers, Phys. Rev. B 105 (2022), 134108, https://doi.org/10.1103/ PHYSREVB.105.134108/FIGURES/6/MEDIUM.
- [85] A.I. Khan, T. Chakraborty, N. Acharjee, S. Subrina, Stanene-hexagonal boron nitride heterobilayer: structure and characterization of electronic property, Sci. Rep. 7 (2017) 1–10, https://doi.org/10.1038/s41598-017-16650-5.
- [86] M.S. Hasan Khan, M.S. Islam, M.R. Islam, A. Iskanderani, I.M. Mehedi, M.T. Hasan, Potential visible-light driven PtO2/GaN vdW hetero-bilayer photocatalysts for water splitting using first-principles, IEEE Access 9 (2021) 109510–109521, https://doi.org/10.1109/ACCESS.2021.3102190.
- [87] M.S.H. Khan, M.R.M.S. Islam, M.R.M.S. Islam, I.M. Mehedi, M.T. Hasan, Tunable photocatalytic properties of planar GaN/GeC hetero-bilayer: production of H fuel, IEEE Access 8 (2020) 209030–209042, https://doi.org/10.1109/ ACCESS 2020 3037036
- [88] J. Li, T. Lei, J. Wang, R. Wu, J. Zhao, L. Zhao, Y. Guo, H. Qian, K. Ibrahim, Anisotropic electronic structure and interfacial chemical reaction of stanene/Bi 2 Te 3, the journal of physical chemistry C. 124 (2020) 4917–4924. 10.1021/acs.jpcc. 0c00139.
- [89] M.I. Kholil, M.T. Hossen Bhuiyan, Effects of Cr- and Mn-Alloying on the Band Gap Tuning, and Optical and Electronic Properties of Lead-Free CsSnBr3 Perovskites For Optoelectronic Applications _ Enhanced Reader.pdf, The Royal Society of Chemistry, 2020, https://doi.org/10.1039/D0RA09270C.
- [90] J. Islam, A.K.M.A. Hossain, Narrowing Band Gap and Enhanced Visible-Light Absorption of Metal-Doped Non-Toxic CsSnCl3 Metal Halides For Potential Optoelectronic Applications, The Royal Society of Chemistry, 2020, https://doi. org/10.1039/c9ra10407k.
- [91] M.I. Kholil, M.T.H. Bhuiyan, M.A. Rahman, M.S. Ali, M. Aftabuzzaman, Influence of molybdenum and technetium doping on visible light absorption, optical and electronic properties of lead-free perovskite CsSnBr3 for optoelectronic applications, RSC Adv. 11 (2021) 2405–2414, https://doi.org/10.1039/ DORA09853A
- [92] M.S.R. Islam, M.S.R. Islam, A.F. Mitul, M.R.H. Mojumder, A.S.M.J. Islam, C. Stampfl, J. Park, Superior tunable photocatalytic properties for water splitting in two dimensional GeC/SiC van der Waals heterobilayers, Sci. Rep. 11 (2021) 1–14, https://doi.org/10.1038/s41598-021-97251-1.
- [93] M.C. Toroker, D.K. Kanan, N. Alidoust, L.Y. Isseroff, P. Liao, E.A. Carter, First principles scheme to evaluate band edge positions in potential transition metal oxide photocatalysts and photoelectrodes, Phys. Chem. Chem. Phys. 13 (2011) 16644–16654, https://doi.org/10.1039/C1CP22128K.
- [94] I. Neri, M. López-Suárez, S. Caponi, M. Mattarelli, Fast MoS 2 thickness identification by transmission imaging, Appl. Nanosci. 11 (2021) 605–610, https://doi.org/10.1007/S13204-020-01604-7/FIGURES/6. Switzerland.
- [95] P.A. Schultz, Theory of defect levels and the "band gap problem" in silicon, Phys. Rev. Lett. 96 (2006), 246401, https://doi.org/10.1103/ PHYSREVLETT.96.246401/FIGURES/3/MEDIUM.
- [96] P.A. Schultz, First principles predictions of intrinsic defects in aluminum arsenide, AlAs, in: Mater. Res. Soc. Symp. Proc. (2011) https://doi.org/10.1557/ onl.2011.765
- [97] J. Zhang, Y. Zhao, X. Guo, C. Chen, C.L. Dong, R.S. Liu, C.P. Han, Y. Li, Y. Gogotsi, G. Wang, Single platinum atoms immobilized on an MXene as an efficient catalyst for the hydrogen evolution reaction, Nat. Catal. 1 (2018) 985–992, https://doi.org/10.1038/s41929-018-0195-1.